Computers and Geotechnics 133 (2021) 104045

Contents lists available at ScienceDirect

Computers and Geotechnics

journal homepage: www.elsevier.com/locate/compgeo

Research Paper

A full-scale in situ heating test in Callovo-Oxfordian claystone: observations, analysis and interpretation

S. Tourchi[a], J. Vaunat[a], A. Gens[a,*], F. Bumbieler[b], M.-N. Vu[b], G. Armand[c]

[a] Universitat Politècnica de Catalunya (UPC) – Centre Internacional de Mètodes Numèrics en Enginyeria (CIMNE), Barcelona, Spain
[b] Agence Nationale pour la Gestion des Déchets Radioactifs (ANDRA), Châtenay-Malabry, France
[c] Agence Nationale pour la Gestion des Déchets Radioactifs (ANDRA), Meuse/Haute Marne Underground Research Laboratory, Bure, France

ARTICLE INFO

Keywords:
In situ heating test
COx claystone
Numerical modelling
THM coupling
Radioactive waste disposal
Temperature effects

ABSTRACT

The paper describes the performance, observations and numerical interpretation of a full-scale in situ heating test conducted on Callovo-Oxfordian (COx) claystone in the Meuse / Haute-Marne (MHM) Underground Research Laboratory (URL) simulating a heat-emitting, high-level radioactive waste disposal concept. In the experiment, five heaters 3 m-long are placed in the axis of a microtunnel excavated in COx claystone to simulate the heat production of radioactive waste. The test is fully instrumented, and attention is focused on the near-field region's thermo-hydro-mechanical (THM) behaviour consisting of the casing surrounding the heater and the host formation (COx claystone). The interpretation of the test is assisted by the performance of a numerical analysis based on a coupled formulation incorporating the relevant THM phenomena. The calculations have used a constitutive law especially developed for this type of material. Initial and boundary conditions for analysis as well as material parameters are determined from a comprehensive field and laboratory experimental programme. The paper presents and discusses the thermal, hydraulic and mechanical observations in COx claystone, casing and an annular air-filled gap between the host formation and the casing. Special attention is also paid to the mechanisms involved in the interface between the rock and the casing. Heating has been applied in two stages; a cooling stage (also applied in steps) completes the experiment. The numerical analysis performed has proved able to represent the progress of the experiment very satisfactorily. By performing the 3D numerical analysis, it has been possible to incorporate anisotropies of material parameters and of in situ stresses. The performance and analysis of the in situ test have significantly enhanced the understanding of a complex THM problem and have proved the capability of the numerical formulation to provide adequate modelling capacity.

1. Introduction

Currently, deep geological disposal is generally accepted as a safe and feasible disposal method of high-level radioactive waste (HLW) (IAEA, 2003). The principle of geological disposal of radioactive waste is to place carefully prepared and packaged nuclear waste in excavated tunnels in geological formations such as salt, hard rock, or clay (Kim et al., 2011). Several organisations have built underground research laboratories (URLs) to carry out research related to geological disposal. These programmes have included large-scale in situ heating tests to study aspects of the full-scale behaviour of the proposed repositories. The CACTUS, ATLAS, and CERBERUS tests (Picard et al., 1994; Bernier and Neerdael, 1996; De Bruyn and Labat, 2002; François et al., 2009) were performed in the Boom clay at the HADES underground research facility in Mol, Belgium and the HE-B, HE-D and HE-E tests were carried out in the Mont Terri laboratory in Northern Switzerland, constructed in Opalinus clay (Gens et al., 2007). The TER and TED heating tests were carried out in Bure at the Meuse/Haute Marne laboratory located in Eastern France (Gens et al., 2011; Conil et al., 2020), constructed in the Callovo-Oxfordian (COx) claystone.

A full-scale in situ heating experiment (ALC1604) representative of the French concept for HLW disposal cell was emplaced in 2012 by Andra (French National Radioactive Waste Management Agency) in COx claystone at the main 490 m deep level of the Meuse/Haute-Marne (MHM) URL in Eastern France). It involved the excavation of a small diameter tunnel and the emplacement of 5 heaters with a total length of 15 m between 10 m and 25 m from the access drift wall. The heaters are placed inside a steel casing and a gap exists initially between the host

---

* Corresponding author.
E-mail address: antonio.gens@upc.edu (A. Gens).

https://doi.org/10.1016/j.compgeo.2021.104045

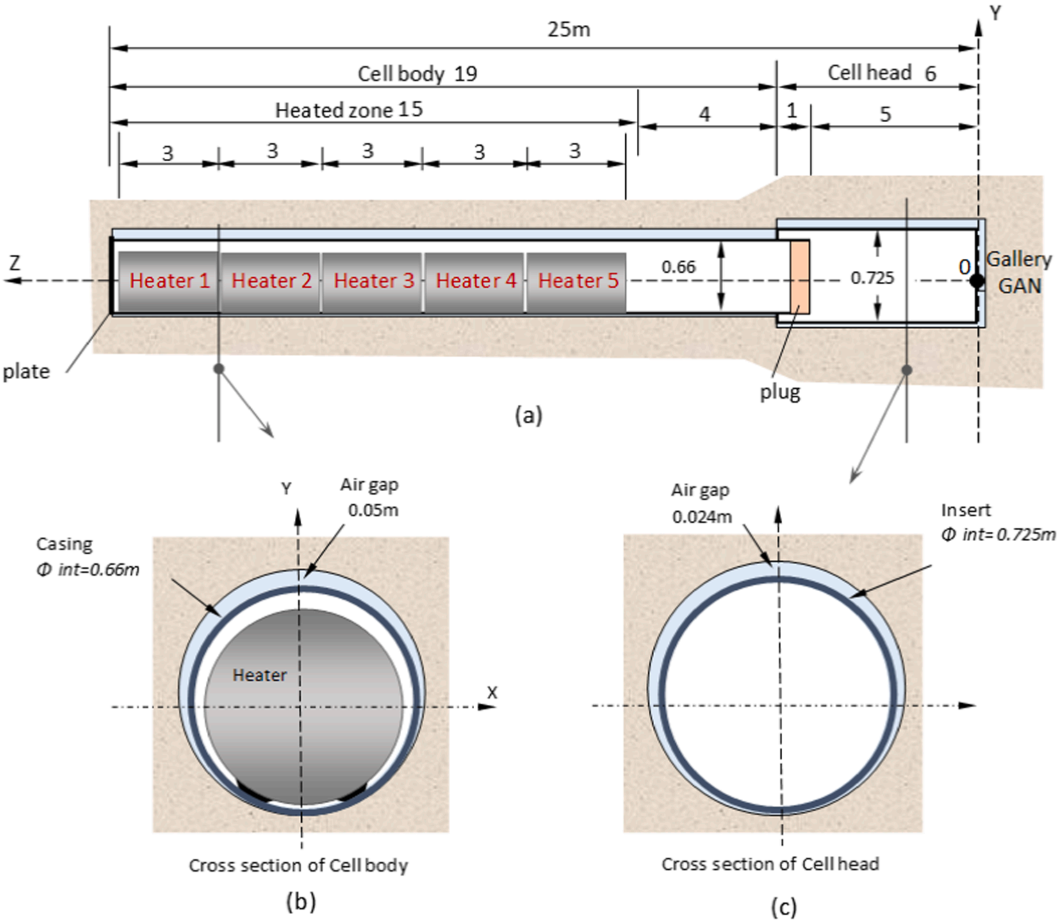

Fig. 1. Layout of ALC1604 in situ test: a) Longitudinal view, b) cross sections of cell body, c) cross section of the cell head.

formation and the casing. A description of the construction and performance of the test are given in Bumbieler et al. (2021). In the current paper, focus is placed on the numerical analyses of the case and on the interpretation of the test observations based on the results of the simulations carried out.

The paper presents an advanced 3D coupled THM numerical modelling of the test intended to assist in the proper interpretation of the observations of the experiment. The paper starts with a description of the design and construction of the test. Afterwards, the coupled THM formulation and constitutive models used in the analysis is briefly outlined. The features of the numerical model and the determination of material parameters are then described. The paper continues with the presentation of some selected observations, and the corresponding results of the numerical analysis. The comparison between predictions and

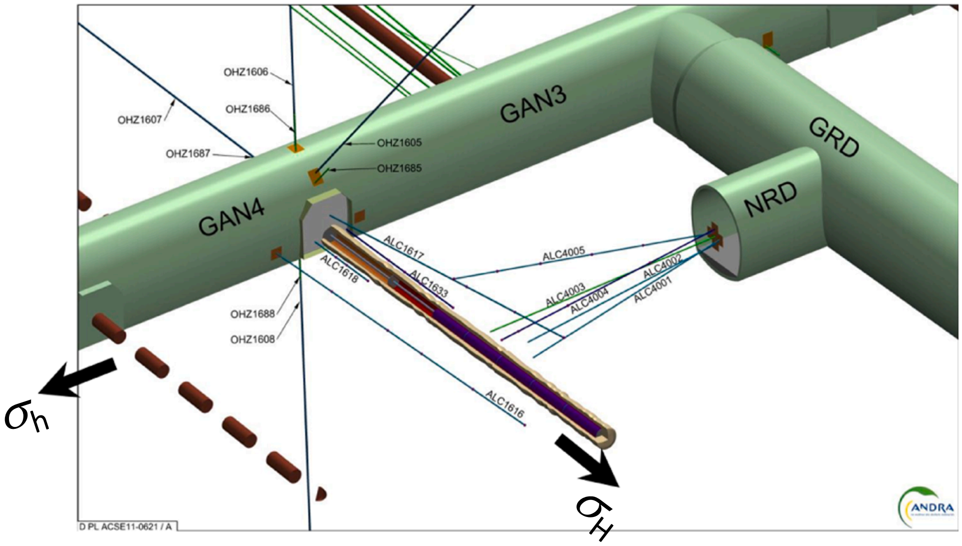

Fig. 2. Schematic layout of ALC1604 in situ test. Locations of observation boreholes drilled from niche NRD and gallery GAN are shown (Andra, 2013).

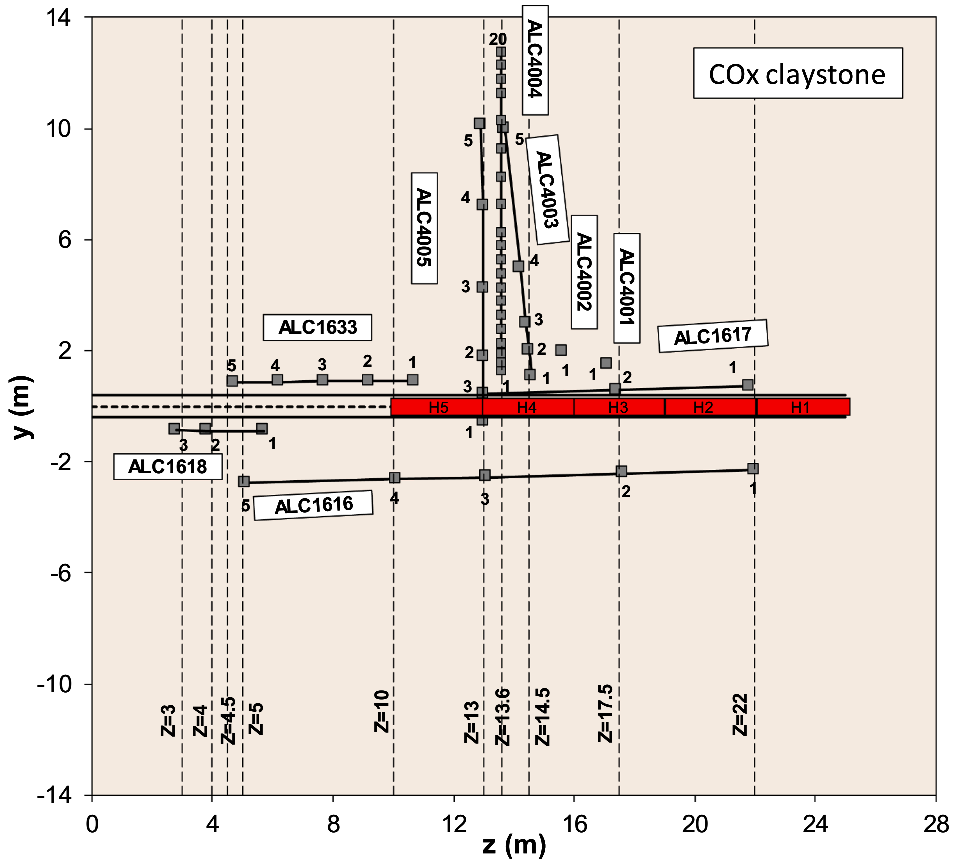

Fig. 3. Location of all observation points in the ALC1604 in situ test. Plan view on a horizontal plane.

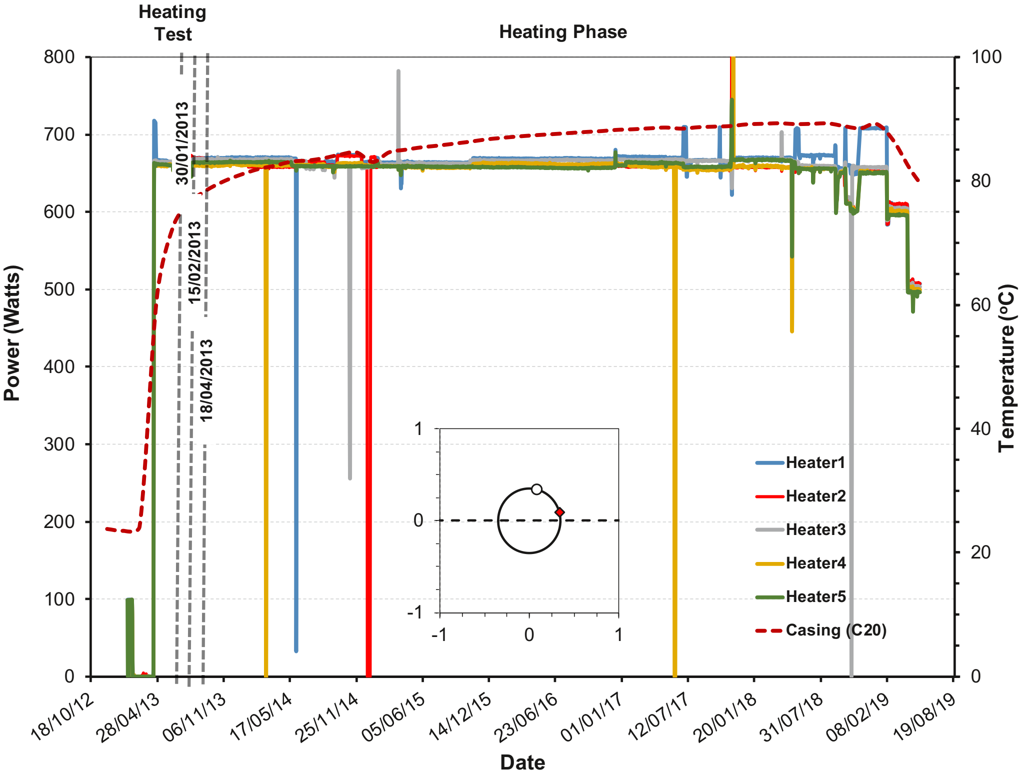

Fig. 4. History of power of heaters (H1-H5) and maximum steel casing temperature of steel during the experiment. Location of temperature measurement sensors on the casing is shown.

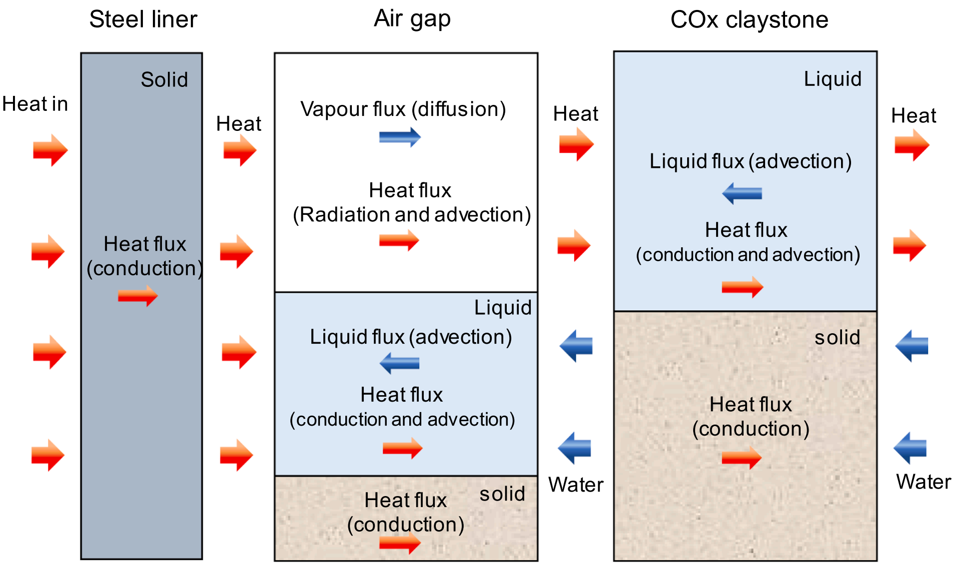

Fig. 5. Scheme of thermo-hydraulic processes in the in situ test.

observations provides a sound basis for the interpretation of the test. Some concluding remarks close the paper.

2. Description of the in situ test

The ALC1604 experiment is an in situ heating test conducted in the Meuse/Haute-Marne (MHM) Underground Research Laboratory (URL) at the main 490 m deep-level where the host formation is Callovo-Oxfordian (COx) claystone (Armand et al., 2017; Bumbieler et al., 2021). The experiment aims to reproduce the initial standard disposal cell for the HLW in France (i.e. without backfilling of annular space between the casing and the rock). It consists of a horizontal microtunnel of approximately 0.7 m in diameter with a reduced length of 25 m (real cells are about 80 m to 150 m long) for the experiment. It comprises a cell body (for HLW disposal), approximately 19 m long, and a 6 m-long cell head section (Fig. 1a). Both cell body and cell head sections incorporate a non-alloy steel casing called Casing and Insert, respectively to ensure retrievability of the waste during at least 100 years (Fig. 1b,c). For the experiment, the cell head is separated from the cell body by steel plate (in real HLW cell, a radiation protection plug will separate both parts of the cell). The far end of the cell is closed off by a plate, also made of non-alloy steel. The diameter of the casing is smaller than that of the insert, and the casing can slide through. Five heaters (H1-H5), each 3 m long and 0.5 m in diameter have been installed contiguously in the body section, as indicated in Fig. 1a. The ALC1604 cell microtunnel was excavated from the GAN gallery at an approximate rate of 0.3–0.5 m/h; the full emplacement (excavation, casing and insert) was completed in 7 days. As indicated in Fig. 2, following the concept for HLW the cell is excavated in the direction of the major principal horizontal stress (Wileveau et al. 2007). The orientation has important implications for the hydro-mechanical response of the rock around the excavations in host formation (Armand et al., 2013; 2014).

The THM behaviour of the COx claystone during the test has been monitored through nine boreholes drilled from the GAN gallery and the NRD niche (Fig. 2) which comprises (Fig. 3):

- Six boreholes with one (ALC4001 and ALC 4002), three (ALC1617 and ALC1618) and five (ALC4005 and ALC 1616) pore pressure piezometer chambers associated with temperature sensors to measure the pressure gradient from the gallery into the rock mass and the pressure evolution near to the heated zone. These boreholes are backfilled with resin to ensure low permeability and compressibility.
- Two boreholes with five temperature measurements (ALC4003 and ALC1633) installed from the gallery niche NRD and gallery GAN, respectively. The boreholes are backfilled with a mix of bentonite and grout to reproduce the characteristics of the rock, mainly its permeability.
- A strain measurement borehole (ALC4004) equipped with 20 extensometers. This borehole is located perpendicular to the heaters, and it is installed from the NRD niche.
- The instrumentation is not concentrated on a single plane, and several sections are available for comparison with numerical results (Fig. 3).

After a short two-week trial step at low power (33 W/m), the main heating phase was started with a constant 220 W/m power along the 15 m occupied by the heater elements. This power was calculated so that a temperature of approximately 90 °C would be reached in the casing after two years. After a heating period of about six years, a staged cooling phase is currently ongoing. Fig. 4 depicts the history of applied power in the test and the evolution of maximum temperature in the casing. As shown in the figure, during the heating stage, the input power has been maintained long enough to achieve a quasi-permanent state. Some short

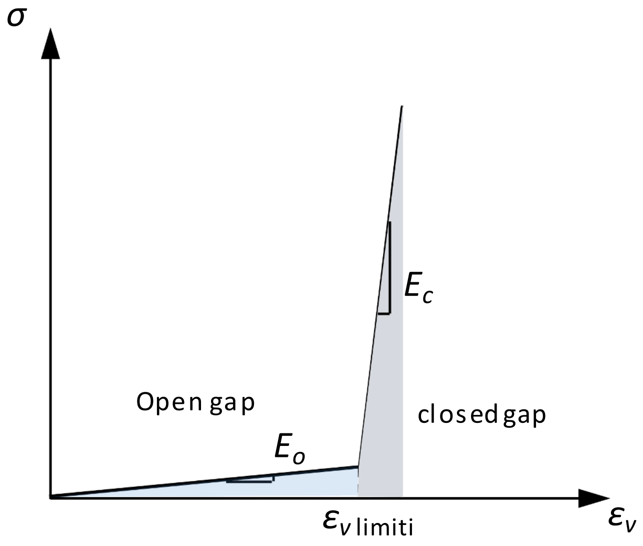

Fig. 6. Bilinear elastic model.

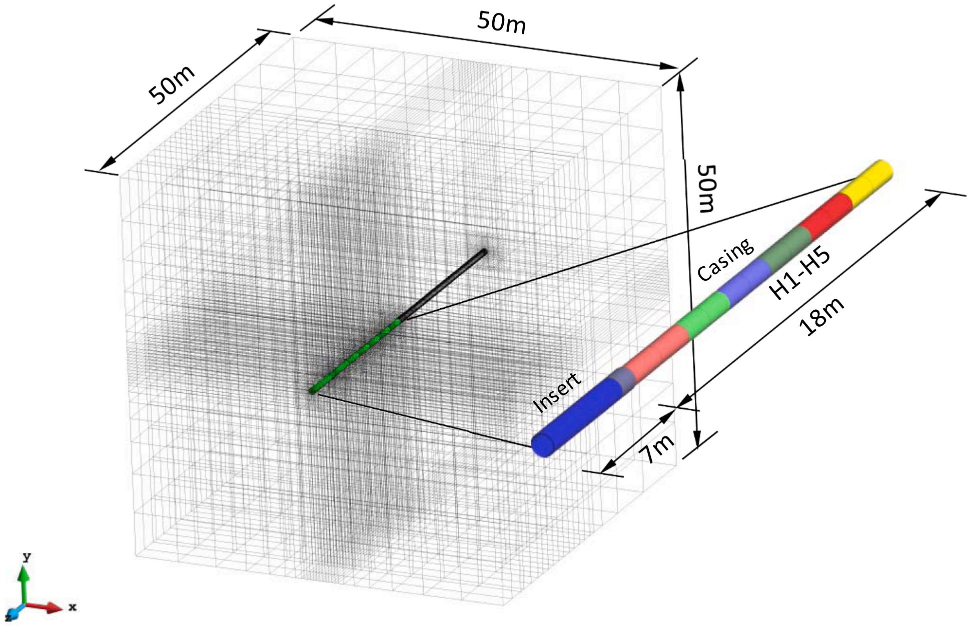

Fig. 7. Finite element mesh three-dimensional analysis. Dimensions are 50 m × 50 m × 50 m. Computation domain centred on the axis of ALC1604 microtunnel.

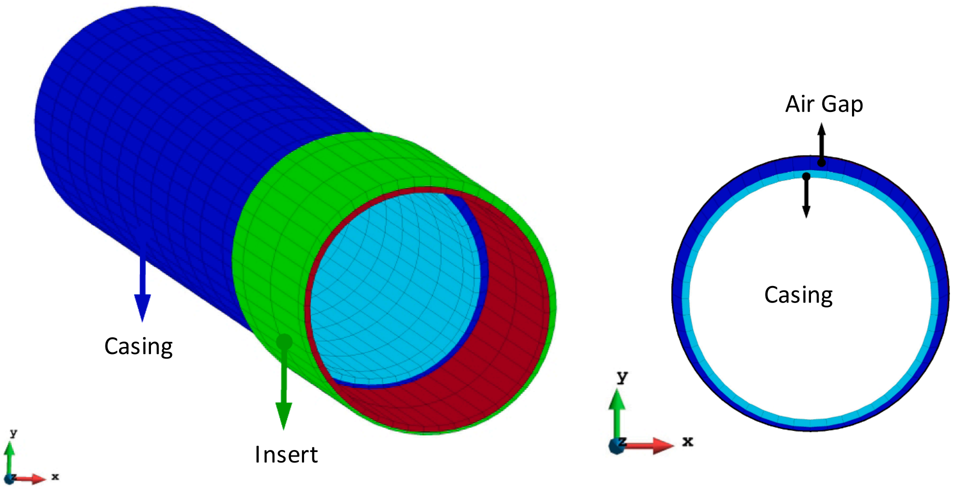

Fig. 8. Three-dimensional view of the mesh close to the casing and cross.section showng the casing and the gap.

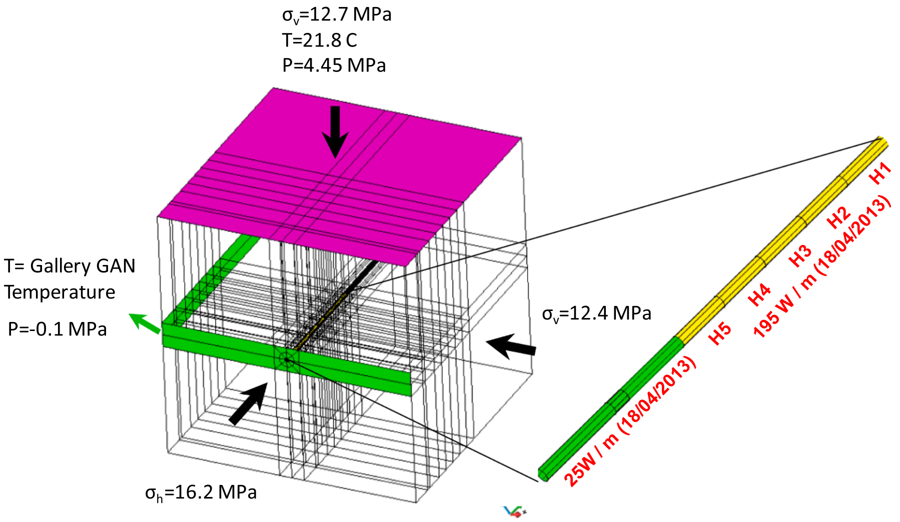

Fig. 9. Initial and boundary conditions applied for 3D THM simulation.

Table 1
Stages of ALC1604 in situ test.

Step	Phase	Date	Duration
1	Galleries GAN-GRD Excavation	September 9, 2010 → October 23, 2012	775 days
2	Microtunnel Excavation	October 23, 2012 → October 31, 2012	56 h
3	Boreholes/Instrumentation	October 31, 2012 → January 30, 2013	94 days
4	Heating Test (30 W/m)	January 30, 2013 → February 15, 2013	16 days
5	Cooling	February 15, 2013 → April 18, 2013	61 days
6	Heating Stage (220 W/m)	April 18, 2013 → February 6 2019	~6 years
7	First cooling phase (200 W/m)	February 6, 2019 → April 8, 2019	61 days
8	Second cooling phase (167 W/m)	April 8, 2019 → June 11, 2019 (planned)	64 days
9	Final cooling phase	June 11, 2019 → August 4, 2025 (planned)	~6 years

Table 2
Callovo-Oxfordian claystone parameters used in the simulations.

properties	Parameter	Orientation*	Value	Reference
Hydraulic	Intrinsic permeability, k_0: m^2	Parallel	$2 \cdot 10^{-20}$	Back-analysis of ALC1604 test
		Perpendicular	$1 \cdot 10^{-20}$	
	Material parameters, η	–	300.	
	Material parameters, λ_0^p	–	$1.2\ 10^{-4}$	
	Model parameter, P : MPa	–	14.3	Wan et al. (2013)
	Material parameters, λ	–	0.33	
	Material parameters, A	–	1.0	
	Material parameters,Λ	–	3.0	
Hydro-mechanical	Biot coefficient, b	–	0.6	Seyedi et al. (2015)
Thermo-mechanical	Linear thermal expansion coefficient of the rock, α_T: K^{-1}	–	$1.4 \cdot 10^{-5}$	Auvray (2004)
	Linear thermal expansion coefficient of the solid grain, α_T: K^{-1}	–	$1.4 \cdot 10^{-5}$	Value and anisotropic ratio from Auvray (2004)
Thermal	Thermal conductivity, λ: W/m/K	Parallel	2.05	Anisotropic back-analysis of thermal field
		Perpendicular	1.33	
	Specific heat capacity of the solid, c_s: J/kg/K	–	800	Auvray (2004)
Petrophysical	Solid compressibility, β_s	–	$2.5 \cdot 10^{-5}$	From mineral composition
	Specific weight, ρ_s: kg/m3	–	2.7	Reference value
	Porosity, ϕ	–	0.173	(Martin and Lanyon 2003)

. * Orientation with respect to bedding.

Table 3
Mechanical constitutive law parameters used in the simulations.

Parameter	Value	Parameter	Value
Young's modulus (Parallel), E: MPa	5200	Constant that controls the curvature of the function in the softening branch,a_{soft}	0.07
Young's modulus (Perpendicular), E: MPa	4000	Coefficient of non-associativity,ω	0.6
Poisson's ratio (Parallel), ν	0.25	Equivalent plastic strain at which the maximum strength is reached,ξ_1	0.005
Poisson's ratio (Perpendicular), ν	0.35	Equivalent plastic strain at which the residual strength is reached,ξ_3	0.006
Rate independent mechanism		Rate dependent mechanism	0.06
Peak friction angles, φ_{peak}: °	22.0	The threshold from which viscoplastic strains are activated,σ_s: MPa	4.0
Initial friction angles, φ_{ini}: °	9.35	Viscosity parameter,γ: day^{-1}	$1x10^{-7}$
Mobilized friction angles, φ_{res}: °	14.74	Material constants,n	3.37
peak cohesion,c_{peak} : MPa	3.55	Material constants,m	530
Constant that controls the curvature of the function in the hardening branch,a_{hard}	0.0035	Scaling factors, c_N	1.33
		Scaling factors, c_S	1.0

Table 4
Casing properties adopted in the analysis.

Properties	Parameter	Value	Reference
Thermal	Thermal Conductivityλ: W/m/K	80	
	Specific heat of solid: J/kg/K	550	Specifications API5LX65 MS non-alloy steel (Bumbieler et al. 2015)
Mechanical	Linear Thermal expansion coefficient, α_T: K^{-1}	$1.4\ 10^{-5}$	
	Young's Modulus, E: MPa	210,000	
	Poisson's ratio, ν	0.3	

power outage episodes have occurred during the experiment; however, they have had a negligible influence on the temperature evolution in the COx claystone and only short temporary effects on the evolution of the casing temperature.

Some of the most important features that make this experiment different from previous ones performed at the Meuse/Haute-Marne URL (Armand et al. 2017) are the large length of the heated zone, the presence of a steel casing around the heaters and the presence of a gap between the casing and the rock.

3. Theoretical formulation

3.1. Coupled phenomena and THM formulation

A considerable number of coupled THM processes are expected to occur in the operation of a high-level nuclear waste (HLW) repository (Gens et al., 2002). In particular, the behaviour of the COx claystone under thermal loading has to be considered in the framework of THM

Table 5
Air-gap element properties adopted in the analysis.

Properties	Parameter	Value	
Thermal	Thermal Conductivityλ_{dry}: W/m/K	0.035	Back-analysis of ALC1604 test
	Thermal Conductivity, λ_{sat}: W/m/K	0.6	
Hydraulic	Intrinsic permeability, k_0: m^2	10^{-16}	
	Porosity,ϕ_0	0.8	
	Parameter for van Genuchten model,λ	0.5	
	Parameter for van Genuchten model, P_0: MPa	0.001	
	material parameter, a	10	
Mechanical	Young's Modulus, E_c: MPa	1000	
	Young's Modulus, E_o: MPa	1.0	
	Strain limit,$\varepsilon_{v\ \mathrm{limit}}$	Variable 0.005 – 0.21	
	Poisson's ratio, ν	0.3	

.

couplings as the various THM phenomena interact. Of course, the strength and significance of each coupling relationship vary widely depending on the problem considered (Bai and Abousleiman, 1997; Zimmerman, 2000). Olivella and Gens have developed conceptual and mathematical models for coupled THM processes since the early 1990 s. This section will discuss the THM aspects of the in situ heating test, concentrating on heat and mass transport phenomena. A review of the physical processes and mechanisms thought to take place during the heating of a low permeability stiff porous medium are first summarised. Then the theoretical formulation of the coupled THM processes that take place during the heating in a porous medium using a multi-phase, multi-species approach (Olivella et al., 1994) is reviewed. Afterwards, a coupled THM formulation is described in some detail; it provides a rational basis for the proper simulation of the various THM phenomena and their interactions.

3.1.1. Thermal processes

The French concept of disposal for HLW expects a maximum temperature of up to 90 °C within the host formation. Heat output from the heaters will dissipate into the surrounding host formation which is the COx claystone. In the context of ALC1604 experiment, under high temperature, THM processes will be generated in the air-filled gap between the casing and the COx claystone and in the host formation. Naturally, the magnitude of applied heating power will control the temperature level of the system. In the rock, heat transport takes place almost exclusively by conduction. Heat advection is negligible as the fluid fluxes are small due to the low hydraulic conductivity of the COx claystone. Thus, heat capacity and thermal conductivity of host formation largely control the near field heat dissipation.

Radiation heat transport takes place in the gap between the host formation and casing and it is active only when the gap remains open. In addition, as the heated zone in the deposition cell is not isolated, there is advective heat transfer through the air present in the cell. An important process from a thermal point of view is gap closure. An open and dry gap has a high isolation potential due to its low thermal conductivity. However, when the gap closes and host formation is in contact with the steel casing, the rate of heat transport naturally increases. Closure of the gap in the experiment was relatively fast (as measured by three rock/casing clearance sensor sectors), test observations indicate that occurred about 400 days after cell excavation.

Consequently, the local thermal response is strongly dependent on the evolution of the air gap. At a more global scale, it has been observed that there are some limited effects of the seasonal variation of temperature in the GAN gallery and the NRD niche.

3.1.2. Hydraulic processes

Thermally-induced excess of pore fluid pressures (or thermal pressurization) is a key phenomenon affecting argillaceous rocks, mainly due to the differential rate of expansion of the skeleton of the argillaceous material, the solid phase ($\sim 1.4 \cdot 10^{-5}$ K^{-1} for COx claystone) and the pore liquid ($\sim 2.3 \cdot 10^{-4}$ K^{-1} at 20 °C and $\sim$ $7.2 \cdot 10^{-4}$ K^{-1} at 90 °C for water). The pore pressure rise may be high in stiff materials and may approach or even exceed hydraulic fracture conditions. Due to the pore pressure rise, high hydraulic gradient is observed and conduct to pore pressure dissipation.

Other thermo-hydraulic processes occurring in the ALC1604 test in the vicinity of the heaters are shown in Fig. 5, in a schematic way. At the inner boundary, the steel casing receives the heat flux from the heaters. The hydraulic gradients induced by the open excavation and the thermal gradients due to the heating are the main drivers for the transient flow phenomena. Water will move from the host formation towards the gap and eventually, hydration should lead to saturation of the air-filled gap

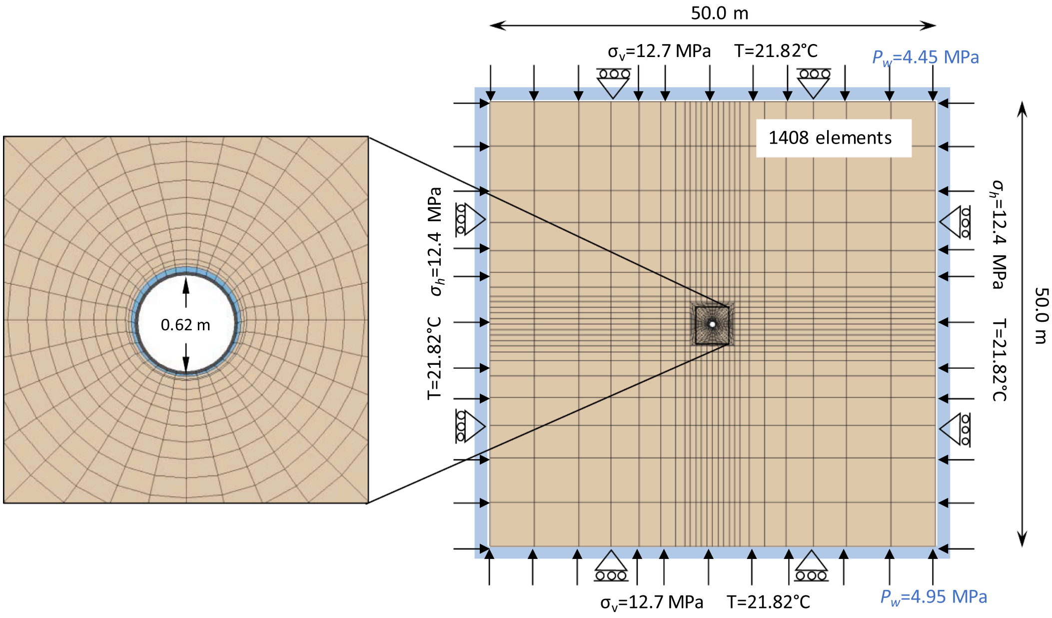

Fig. 10. Domain modelled, finite element mesh and boundary conditions used in 2D analyses A1 and A2.

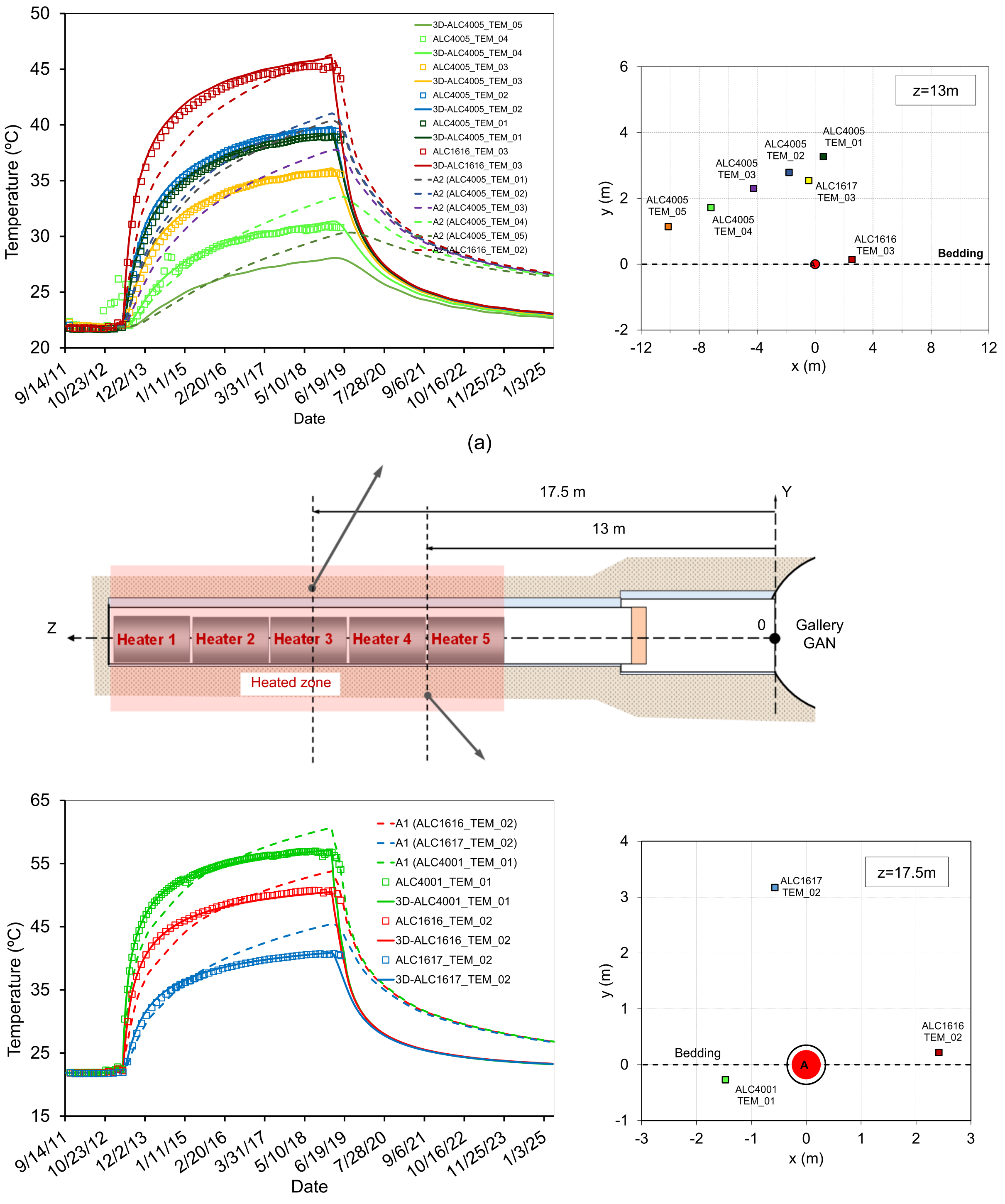

(a)

(b)

Fig. 11. Evolution of temperatures in COx claystone, observations and computed results: (a) Section z = 17.5 m; (b) section z = 13 m.

unless it closes before. Vapour will be present in the gas phase in the gap at equilibrium with local temperature and suction.

3.1.3. THM formulation and balance equations

The coupled THM formulations used in this work has been described previously in (Olivella et al. 1994; Gens et al. 1998; Gens and Olivella, 2000; Gens et al., 2011) and it will only be outlined herein. It is based on a multi-phase, multi-species approach. A general balance equation contains three terms: the change with time of a property of the porous material, the divergence of the flux of this property and the rate of production/decay of the property:

$$\frac{\partial}{\partial t}(\rho\cdot\psi)+\nabla\cdot(j_{\psi})-f^{\psi}=0 \qquad (1)$$

where $\psi$is the property per unit mass, ρ is density, j_{ψ} is the total mass flux of ψ and f^{ψ} is the rate of production/decay of ψ per unit volume.

Using a compositional approach, the volumetric mass of a species in a phase θ_{ψ} is the product of the mass fraction of that species, ω_{ψ}, and the

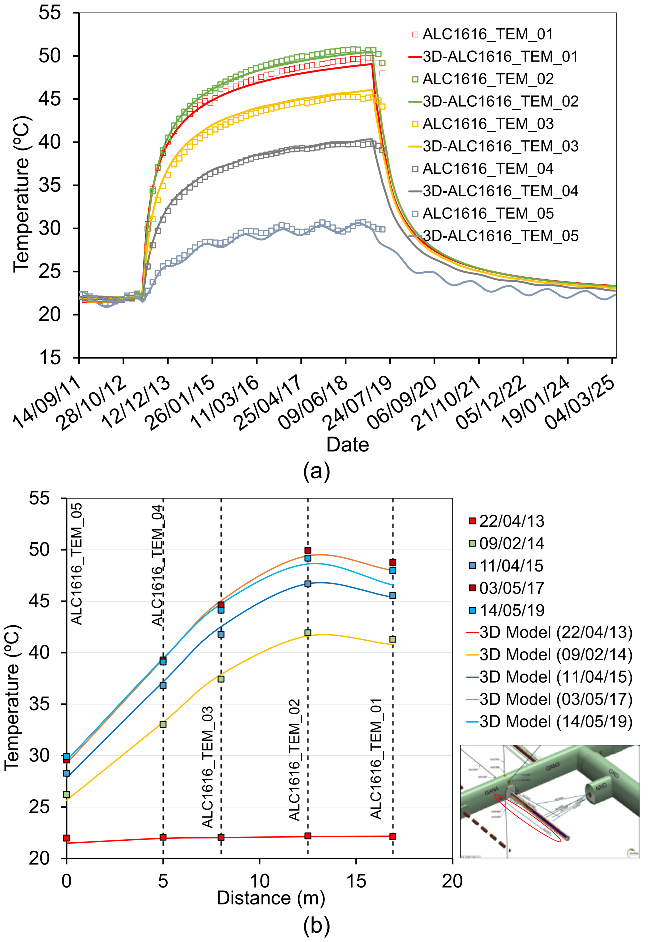

(a)

(b)

Fig. 12. Temperature evolution of the sensors of the borehole ALC1616. The measurements (dots) are compared to the simulation results (lines).

bulk density of the phase, ρ.

As water is present in liquid and gas phases, the total mass balance of water is expressed as:

$$\frac{\partial}{\partial t}\left(\theta_l^w S_l \phi + \theta_g^w S_g \phi\right) + \nabla\cdot\left(\boldsymbol{j}_l^w + \boldsymbol{j}_g^w\right) = f^w \tag{2}$$

where θ_l^w and θ_g^w are the mass content of water per unit volume of liquid and gas, respectively. S_l and S_g are the degree of saturation of liquid and gaseous phases, respectively and ϕ is the porosity. $\boldsymbol{j}_l^w$ and $\boldsymbol{j}_g^w$ are the total water mass fluxes in the liquid and gas phases concerning a fixed reference system and f^w is a source/sink term of water. Using the material derivative leads to the following expression of the mass water balance:

$$\phi\frac{D_s}{Dt}\left(\theta_l^w S_l + \theta_g^w S_g\right) + \left(\theta_l^w S_l + \theta_g^w S_g\right)\frac{D_s\phi}{Dt} + \left(\left(\theta_l^w S_l + \theta_g^w S_g\right)\phi\right)\nabla\hat{A}\cdot\frac{d\mathbf{u}}{dt} + \nabla\hat{A}\cdot\left(\mathbf{j}_l^{\prime w} + \mathbf{j}_g^{\prime w}\right) = f^w \tag{3}$$

The equation for internal energy balance for the porous medium is established, considering the specific internal energy per unit mass of each phase(E_s, E_l):

$$\frac{\partial}{\partial t}\left(E_s\rho_s(1-\phi) + E_l\rho_l\phi + E_g\rho_g\phi\right) + \nabla\hat{A}\cdot\left(\boldsymbol{i}_c + \boldsymbol{j}_{E_s} + \boldsymbol{j}_{E_l} + \boldsymbol{j}_{E_g}\right) = f^Q \tag{4}$$

where $\boldsymbol{i}_c$ is the energy flux due to conduction through the porous medium, $\boldsymbol{j}_{E_s}$, $\boldsymbol{j}_{E_l}$ and $\boldsymbol{j}_{E_g}$ are advective fluxes of energy caused by mass motions and f^Q is an internal or external energy supply. If inertial terms are neglected, the balance of momentum for the porous medium reduces to the equilibrium equation for total macroscopic stresses:

$$\nabla\cdot\boldsymbol{\sigma} + \boldsymbol{b} = \mathbf{0} \tag{5}$$

where $\boldsymbol{\sigma}$ is the total stress tensor, and $\boldsymbol{b}$ is the vector of body forces.

The main unknowns of the equations are the state variables: solid displacements, $\boldsymbol{u}$ (three spatial directions); liquid pressure P_l; gas pressure P_g; and temperature T.

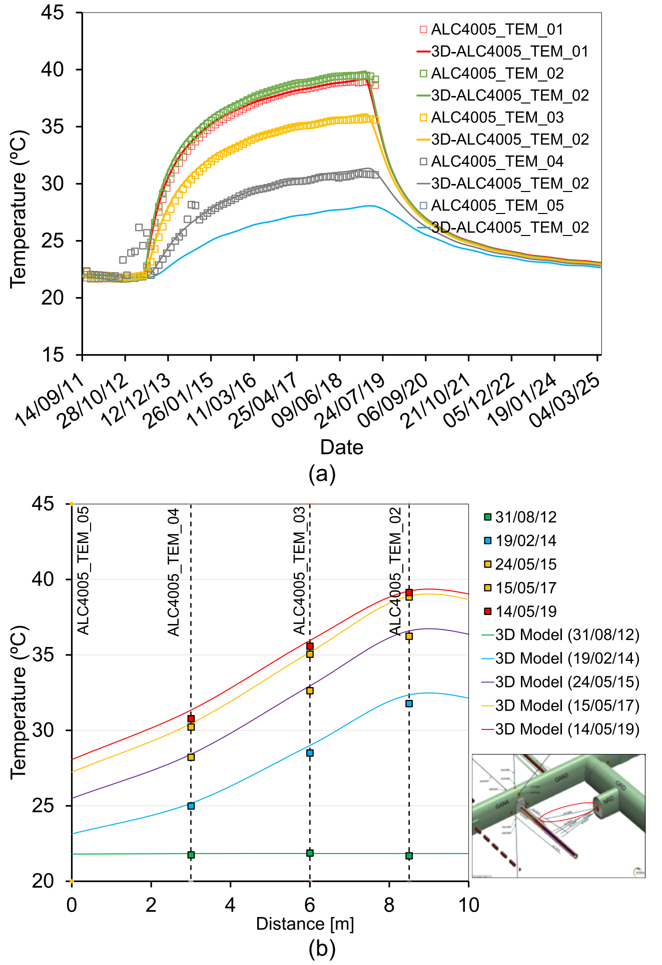

(a)

(b)

Fig. 13. Temperature evolution of the sensors of the borehole ALC4005. The measurements (dots) are compared to the simulation results (lines).

3.1.4. *Mechanical process*

The evolution of temperatures and pore pressure generates stress and strain changes. The thermal problem can also be linked by energy transport through water (hydraulic) convection and energy loss associated with deformation (mechanical) processes.

In situ observations have revealed that excavation operations induce damage and fracturing around the ALC1604 cell, creating an excavation induced fractures network, in which the mechanical and hydraulic properties are modified. Because of its orientation, the tunnel excavation damaged zone extends further in the horizontal direction, suggesting anisotropic characteristics of the rock mass (Armand et al., 2014). The steel casing's mechanical response is also affected by the presence of the EDZ. Due to the larger EDZ development on the horizontal direction, rock convergence in the horizontal direction predominates (Armand et al., 2013).

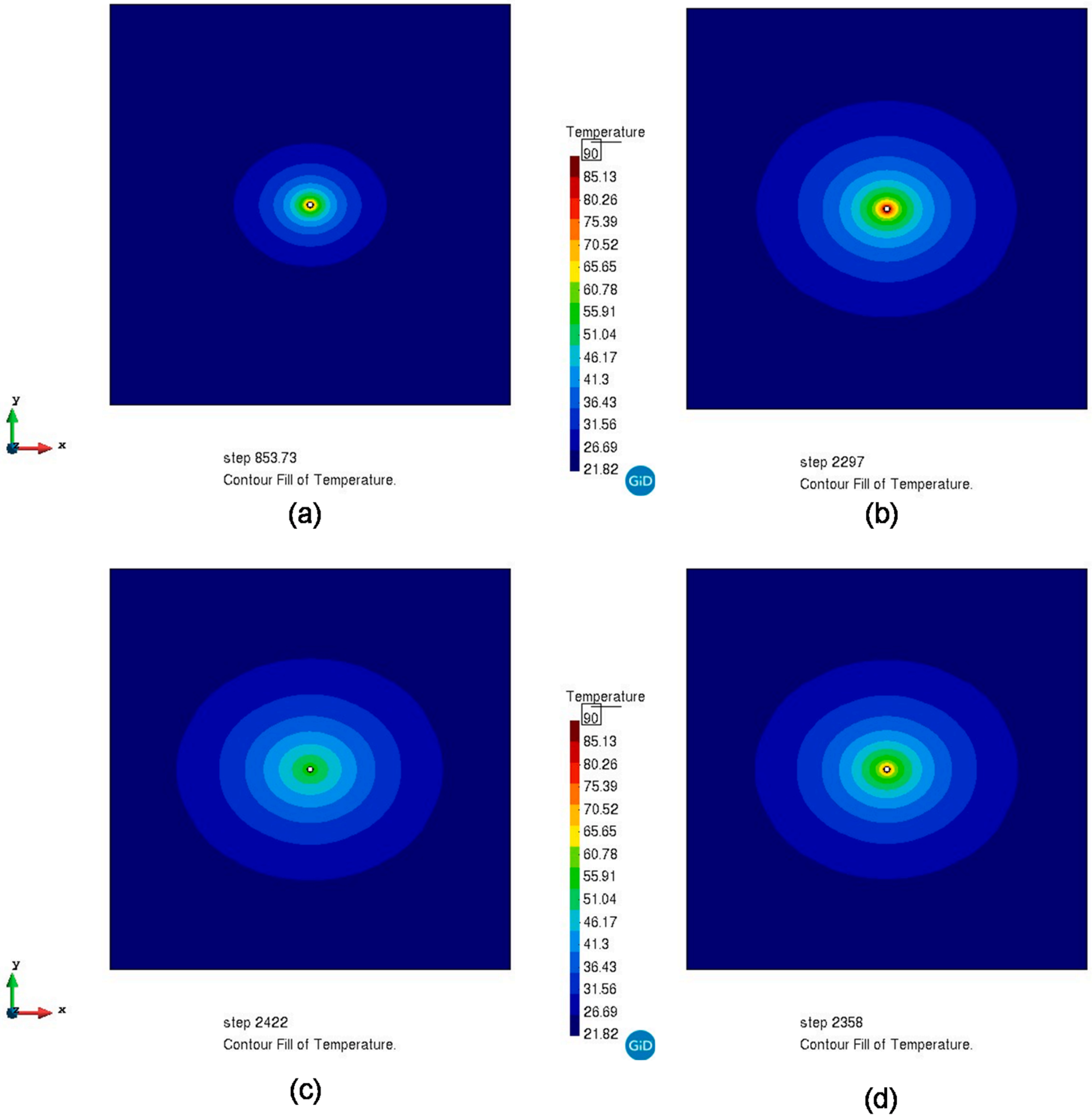

Fig. 14. Computed contours of equal temperature (°C) in section z = 17.5 m for (a) 985 days (two years heating); (b) 2297 days (end of heating); (c) 2358 days (end of first cooling phase); (d) 2422 days (end of second cooling phase).

3.2. Constitutive models

3.2.1. COx claystone

In this section, a constitutive model is described aimed to reproduce the main features of hydromechanical behaviour of the COx claystone. In particular, it incorporates anisotropy of strength and stiffness, nonlinear isotropic hardening to compensate for plastic deformation prior to peak strength, softening behaviour after the peak, a non-associated flow rule time-dependent deformation and permeability dependency on irreversible strains. The model is an enhanced version of the elastoplastic model for partially saturated argillaceous rocks first proposed by (Mánica et al. 2017), which consists of an elasticity law, plastic flow rule, hardening law, and yield condition. The model comprises two main deformation mechanisms: an instantaneous response related to stress changes and a time-dependent response occurring under constant stress.

A generalized effective stress expression has been adopted.

$$\sigma^{'} = \sigma + S_e s B \mathbf{I} \tag{6}$$

where $\sigma^{'}$ is the effective stress tensor, σ is the total stress tensor, S_e is the equivalent degree of saturation (defined below), s is suction, B is Biot's coefficient, and **I** is the identity tensor. In the following, the term "stress" always denotes effective stress.$\sigma^{'}$

The basic formulation of the isotropic elastoplastic model is given here to ensure completeness. The conventional formulation of plasticity can be presented as:

elastic stress–strain relationship

$$\boldsymbol{\sigma} = \mathbf{D}_e\left(\boldsymbol{\varepsilon} - \boldsymbol{\varepsilon}_p\right) \tag{7}$$

Here, $\boldsymbol{\sigma}$ is the column matrix of independent stress components, $\mathbf{D}_e$ is the elastic stiffness matrix, ε is the column matrix of engineering total strain components, ε_p is the column matrix of engineering plastic strain components.

yield condition

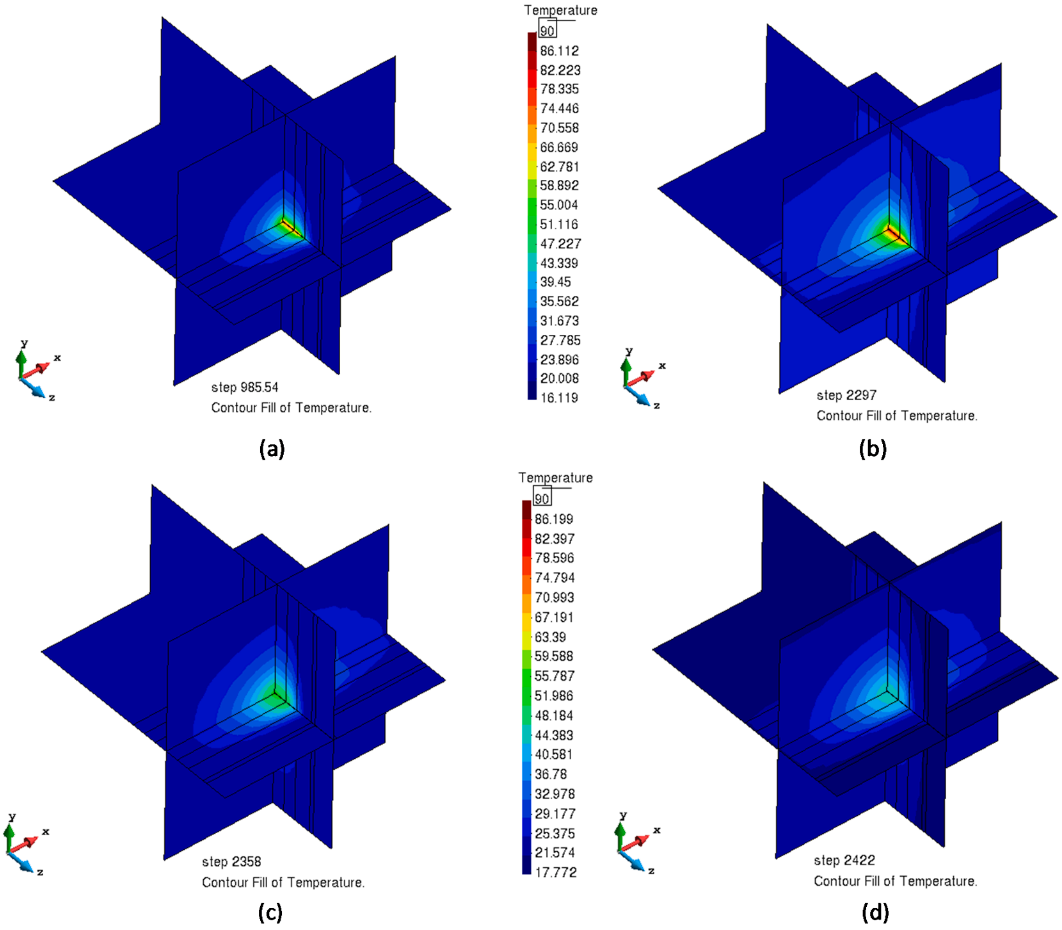

Fig. 15. Three-dimensional views of computed contours of equal temperature (°C) on section A for (a) 985 days (two years heating); (b) 2297 days (end of heating); (c) 2358 days (end of first cooling phase); (d) 2422 days (end of second cooling phase).

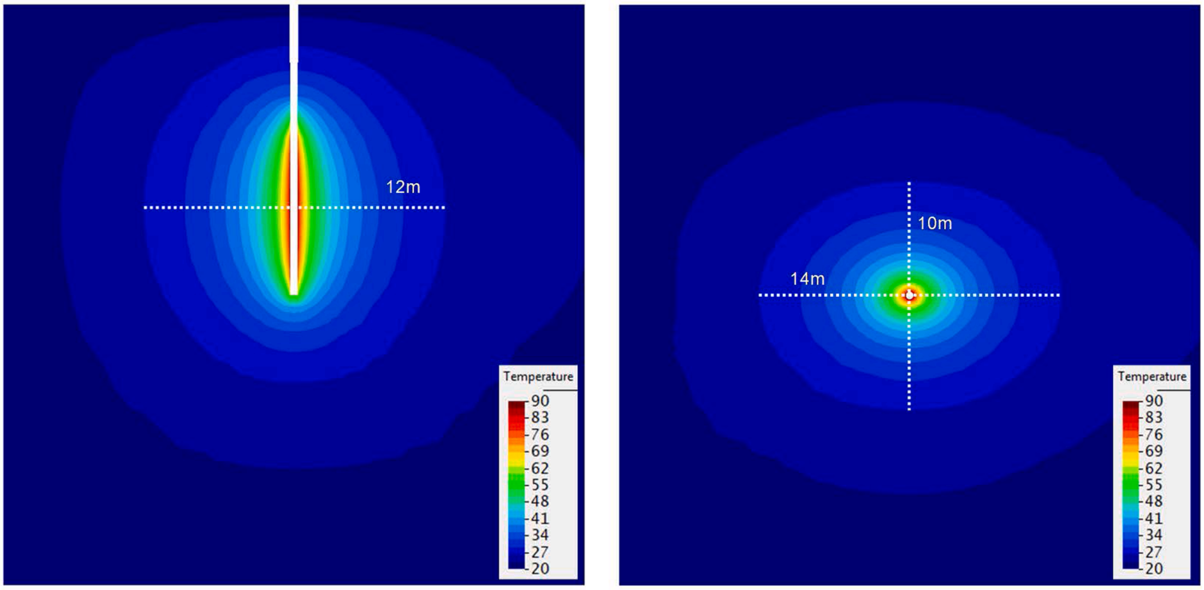

Fig. 16. Calculated temperature distribution in the XZ (left) and XY (right) planes at the end of the heating phase.

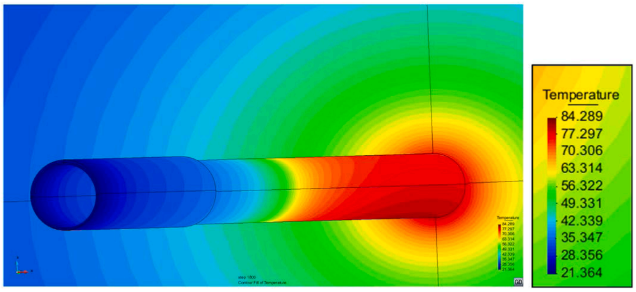

Fig. 17. Three-dimensional view of computed contours of equal temperature in the casing (after two years heating).

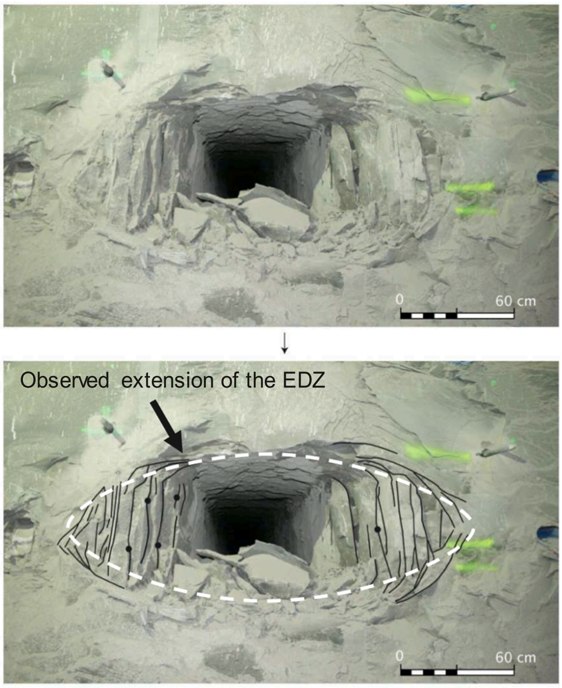

Fig. 18. Extension of the damaged zone around an HLW cell parallel to major horizontal stress, showing the elliptical distribution of fractures around the opening, with a larger extension in the horizontal direction (Armand et al., 2014).

$$f(\boldsymbol{\sigma},\boldsymbol{\gamma})=0 \tag{8}$$

where f is the yield function, γ is a vector of material parameters

flow rule

$$d\varepsilon_p = d\lambda\frac{\partial g}{\partial \boldsymbol{\sigma}} \tag{9}$$

where λ is the plastic multiplier and g is the plastic potential.3.

The instantaneous response is described within the framework of elastoplasticity. Under low deviatoric stresses, the response is linear elastic but characterised through a transverse isotropic form of the Hooke's law. For higher deviatoric stresses, plastic deformations can take place. Initial, peak and residual yield limits are considered. The first one defines a surface in the stress space that separates the elastic and plastic regions, but the material can sustain further loading. The peak limit represents the maximum strength of the material. From this point on, strength is gradually reduced to its residual value modelled through softening plasticity. The Mohr-Coulomb criterion is used for the initial, peak and residual limits, which in terms of commonly employed stress invariants reads:

$$f = \left(cos\theta + \frac{1}{\sqrt{3}}\, sin\theta sin\backslash\varphi\right)J - sin\varphi(ccot\varphi + p^{`}) \tag{10}$$

where p J θ are stress invariants, ϕ is the friction angle and c is the cohesion.

Strain hardening and softening have been taken into account by making the cohesion c and friction angle φ as functions of the equivalent plastic strain ε_{peq}, defined as:

$$\varepsilon^p_{eq} = \left(\frac{2}{3}\varepsilon^p : \varepsilon^p\right)^{1/2} \tag{11}$$

where ε^p is the plastic strain tensor.

Following Mánica et al. (2017), the cohesion c and mobilized friction angle φ increase to a maximum value that accounts for bonding effects before decreasing to a residual value. Afterwards, a gradual reduction takes place until the residual strength is reached at very large displacements. Therefore, $c(\varepsilon_p)$ and $\varphi(\varepsilon_p)$ will be determined based on the initial yield, peak and residual values calibrated from the stress–strain curve obtained in triaxial tests. The mathematical expressions adopted are as follows:

$$\varphi_{mob} = \varphi_{ini} + \frac{\varepsilon^p_{eq}}{a_{hard} + (\varepsilon^p_{eq}/\Delta\varphi_{hard})},\ \Delta\varphi_{hard} = \frac{\xi_1}{\left[\xi_1/\left(\varphi_{peak} - \varphi_{ini}\right)\right] - a_{hard}} \tag{12}$$

$$\begin{aligned}\varphi_{mob} &= \varphi_{peak} + \frac{\varepsilon^p_{eq} - \xi_2}{a_{soft} + \left[(\varepsilon^p_{eq} - \xi_2)/\Delta\varphi_{soft}\right]},\ \Delta\varphi_{soft}\\ &= \frac{\xi_3 - \xi_2}{\left[(\xi_3 - \xi_2)/\left(\varphi_{peak} - \varphi_{ini}\right)\right] - a_{soft}}\end{aligned} \tag{13}$$

whereφ_{mob} = mobilized friction angle, φ_{res} = residual friction angle, ξ_1 = equivalent plastic strain at which the maximum strength is reached, ξ_2 = equivalent plastic strain at which softening begins, ξ_3 = equivalent plastic strain at which the residual strength is reached, a_{hard}= constant that controls the curvature of the function in the hardening stage, a_{soft}= constant that controls the curvature of the function in the softening stage. Cohesion evolves in parallel with the friction angle according to:

$$c_{mob} = c_{peak}cot\varphi_{ini}tan\varphi_{mob} \tag{14}$$

A non-associated flow rule is adopted in the model. Instead of deriving a specific function for plastic potential, the flow rule is obtained from the yield criterion as follows:

$$\frac{\partial g}{\partial \sigma'} = \omega\frac{\partial f}{\partial p}\frac{\partial p}{\partial \sigma'} + \frac{\partial f}{\partial J}\frac{\partial J}{\partial \sigma'} + \frac{\partial f}{\partial \theta}\frac{\partial \theta}{\partial \sigma'} \tag{15}$$

where g is the plastic potential and ω is a constant that controls the volumetric component of plastic deformations.

The model has been extended to consider strength cross-anisotropy through a non-uniform scaling of the stress tensor. This extension is obtained by replacing $p\ J\ \theta$ in Eq. (10) by $p_{ani}\, J_{ani}\ \theta_{ani}$ respectively. These variables are invariants with its usual definition but calculated from the anisotropic stress tensor ($\boldsymbol{\sigma}_{ani}$). This tensor is obtained through the non-uniform scaling of the effective stress tensor oriented with the local coordinate system (σ^{loc}), as shown below

$$\sigma_{ani} = \begin{bmatrix} \dfrac{\sigma^{loc}_{11}}{c_N} & c_s\sigma^{loc}_{12} & \sigma^{loc}_{13} \\ c_s\sigma^{loc}_{12} & c_N\sigma^{loc}_{22} & c_s\sigma^{loc}_{23} \\ \sigma^{loc}_{13} & c_s\sigma^{loc}_{23} & \dfrac{\sigma^{loc}_{33}}{c_N} \end{bmatrix} \tag{16}$$

where c_N and c_S are the normal and shear scaling factors, respectively. An appropriate selection of strength parameters and scaling factors

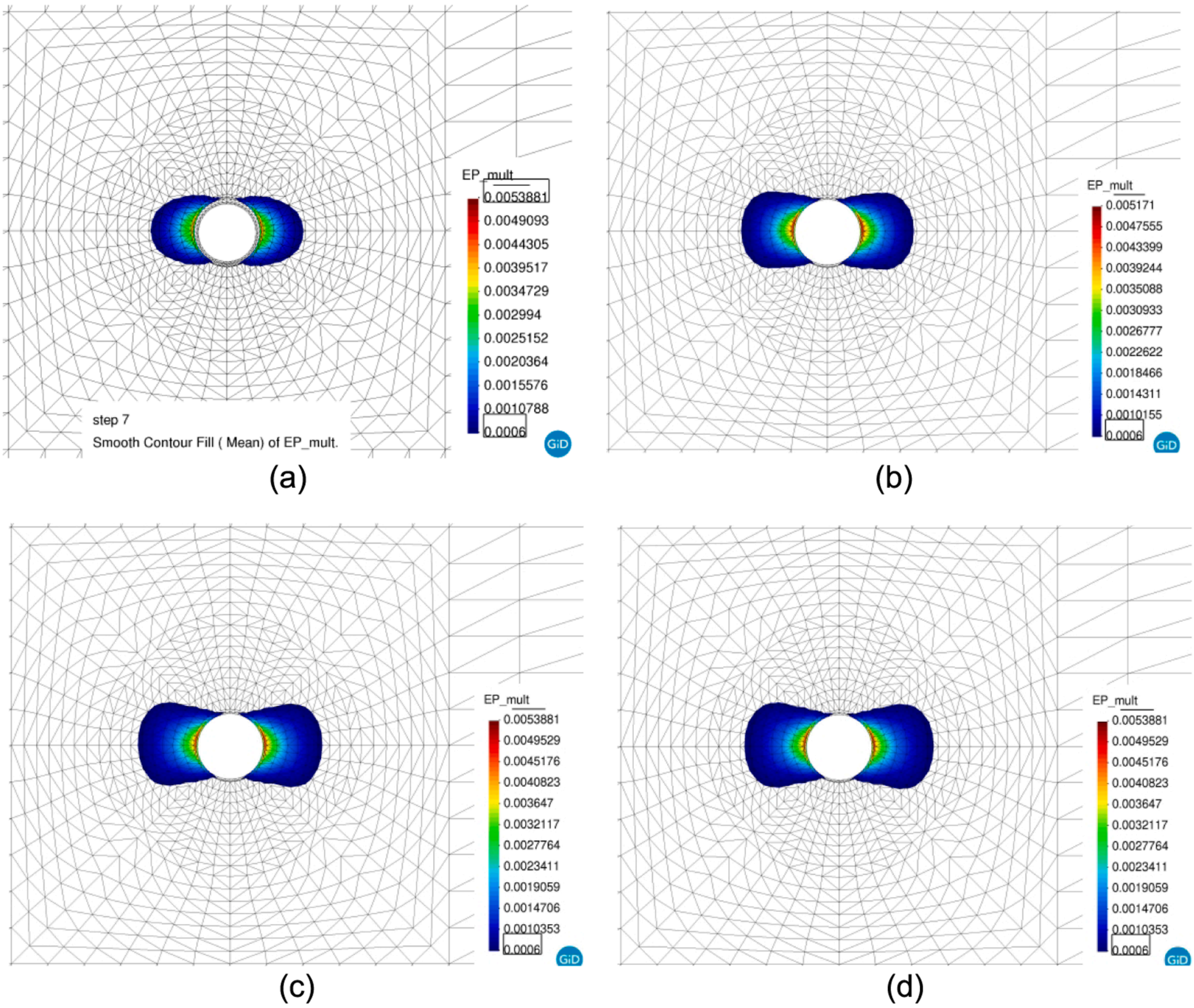

Fig. 19. Obtained configuration of the EDZ in terms of the plastic multiplier in the section z = 17.5 m for (a) 7 days (end of the excavation); (b) 2297 days (end of main heating phase).

allows a satisfactory matching of a specified strength variation with loading orientation. Details about the physical meaning of the anisotropy parameters, their effects, and of the derivation of the corresponding elastoplastic constitutive matrix are given in (Mánica et al. 2016).

An additional mechanism is considered for the time-dependent response, characterized by a modified form of the Lemaitre's law.

$$d\varepsilon^{vp} = \left(\frac{2}{3}\frac{\dot{\varepsilon}^{vp}}{q}s\right)dt \tag{17}$$

$$q = \left(\frac{3}{2}\mathrm{s}:\mathrm{s}\right)^{1/2} \tag{18}$$

$$\dot{\varepsilon}^{vp} = \gamma(q-\sigma_s)^n\left(1-\varepsilon^{vp}_{eq}\right)^m \tag{19}$$

where $d\varepsilon^{vp}$ is the visco-plastic strain increment (time-dependent response), dt is the time increment and $\dot{\varepsilon}^{vp}$ is the visco-plastic strain rate tensor, γ is a viscosity parameter, σ_s is a threshold from which visco-plastic strain is activated, n and m are material constants and ε^{vp}_{eq} is the state variable of the time-dependent response given by:

$$\varepsilon^{vp}_{eq} = \int_0^t\left(\frac{2}{3}\dot{\varepsilon}^{vp}:\varepsilon^{vp}\right)^{1/2}dt \tag{20}$$

Hydraulically, Darcy's law governs fluid flow, as:

$$\boldsymbol{q}_l = \frac{\boldsymbol{k}k_r}{\mu_w}(\nabla P_1 - \rho_1 g) \tag{21}$$

where $\mathbf{k}$ is the intrinsic permeability tensor, k_r is the relative permeability and μ_w is the water viscosity. P_l is the pore fluid pressure and ρ_l is the density of the fluid. The relative permeability is considered a function of porosity and the effective degree of saturation.

In the context of argillaceous rocks, it is necessary to take into account the significant increase of permeability that occurs when the rock experiences fracturing in the Excavation Damaged Zone (EDZ).

In this paper, this feature is incorporated by including a dependency of the intrinsic permeability on the plastic multiplier and defining a threshold value below which permeability does not change. An exponential function has been adopted for the variation of permeability (Tourchi 2020):

$$k = \begin{cases} k = k_0 e^{\eta\left(\lambda^p - \lambda^p_0\right)} \text{ if } \lambda^p > \lambda^p_{tr} \\ k_0 \text{ if } \lambda^p < \lambda^p_{tr} \end{cases} \tag{22}$$

where $k_0$is the intrinsic permeability of the intact rock, η is a constant that controls the rate of change, $\lambda^p$is the cumulative value of the plastic multiplier and λ^{p_0} is a plastic multiplier threshold value.

Although it is likely that the host formation will remain saturated (Armand et al. 2017), the possibility is left open in the analyses by

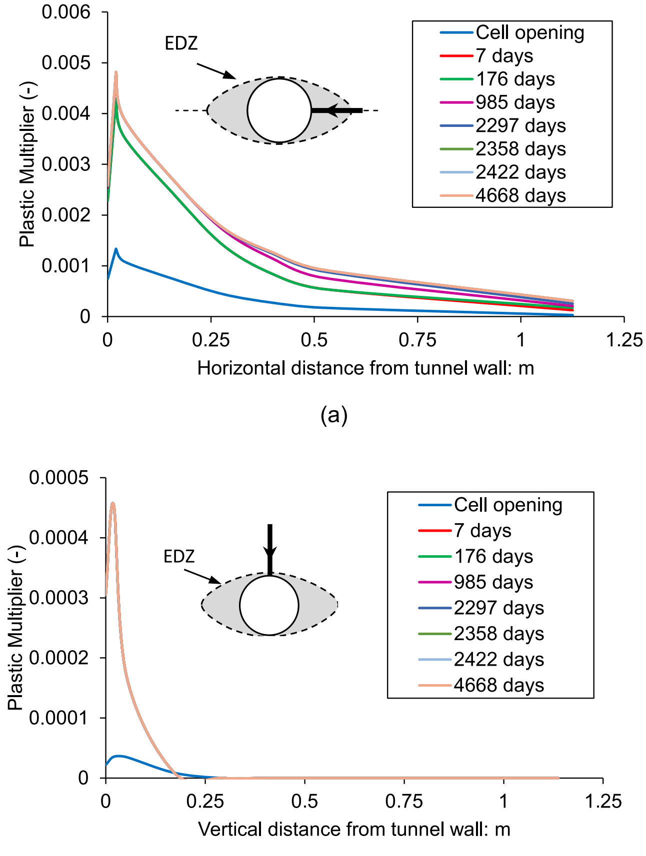

(a)

(b)

Fig. 20. Computed plastic multiplier increment distributions at various times on section perpendicular to Heater 3 (z = 17.5 m) in (a) Horizontal distance to the tunnel wall; (b) Vertical distance to the tunnel wall.

incorporating a liquid phase retention curve and a vapour transport equation.

The Van Genuchten (1980) retention curve is used:

$$S_e = \frac{S_l - S_{rl}}{S_{ls} - S_{rl}} = \left(1 + \left(\frac{P_g - P_l}{P}\right)^{1/(1-\lambda)}\right)^{-\lambda} \tag{23}$$

where S_e, S_l, S_{rl} and S_{ls} are the effective degree of saturation of porous media, degree of saturation of liquid, residual degree of saturation and maximum degree of saturation respectively. P_g and P_l are gas and liquid pressure, respectively and λ is the shape function coefficient of the retention curve. P is a parameter that can be described as air inlet pressure. S_e controls furthermore the relative permeability to water through the following dependency:

$$k_{rl} = A S_e^{\Lambda} \tag{24}$$

Vapour diffusion is governed by Fick's law:

$$i_g^w = -(\tau \phi \rho_g S_g D_g^w \mathrm{I}) \nabla \omega_g^w \tag{25}$$

where i_g^w is the non-advective mass flux vector, ϕ is the porosity of porous media, ρ_g is the density of the gas phase, S_g is the degree of saturation of the gas phase, D_g^w is the coefficient of molecular diffusion for vapour in the gas phase, ω_g^w is the mass fraction g of the gas phase vapour, I is the identity tensor, and τ is a tortuosity coefficient.

The diffusion coefficient of vapour is given by:

$$D_g^w = D^v \frac{(273.15 + T)^n}{P_g} \tag{26}$$

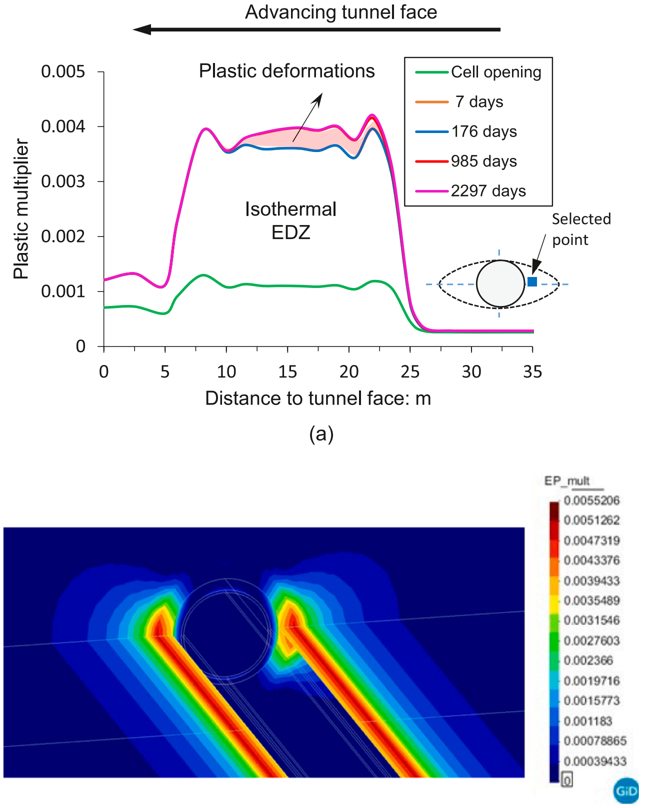

(a)

(b)

Fig. 21. (a) Computed damage distribution at various times in the point with Δx = 4 cm horizontal distance to the tunnel wall; (b) 3D view of computed contours of plastic multiplier (after excavation).

where D^v is the coefficient of diffusion (5.9×10^{-6} m^{2}s^{-1}K^{-n}Pa) of vapour in the air, n is a parameter ($n = 2.3$) and T is the temperature in °C.

Finally, heat conduction is governed by Fourieŕs law, the heat flux vector is:

$$\boldsymbol{i}_c = -\lambda \nabla T \tag{27}$$

3.2.2. Gap element

The mechanical behaviour of the gap has been modelled using a bilinear elastic model that uses two values of Young's modulus, one for the open gap and the other for the closed gap. A large value of Young's modulus (E_c) was used for the closed gap (representing the contact between gap surfaces), and a very low value (E_o) was used for the open gap (Fig. 6). A value of volumetric strain dependent on the initial gap width was used to check whether the gap was open or closed.

From the hydraulic point of view, the gap is modelled as a material with very high porosity and permeability higher by several orders of magnitude compared to the other materials. A porosity value of 1 has not been used to avoid numerical, issues, but the gap behaviour is satisfactory as long as a large value is adopted. Intrinsic permeability is assumed a function of porosity as:

$$k = k_0 \frac{\phi^3}{(1-\phi)^2} \frac{(1-\phi_0)^2}{\phi_0^3} \tag{28}$$

where ϕ_0 is reference porosity and k_0 intrinsic permeability for a matrix with ϕ_0 porosity.

For the gap retention curve, the van Genuchten model is used (Eq. (23)). The retention curve is also considered but with a very low value of the reference air entry pressure, as the gap corresponds to a material with very large pores. This implies that saturation occurs suddenly when capillary pressure vanishes. To avoid numerical convergence problems,

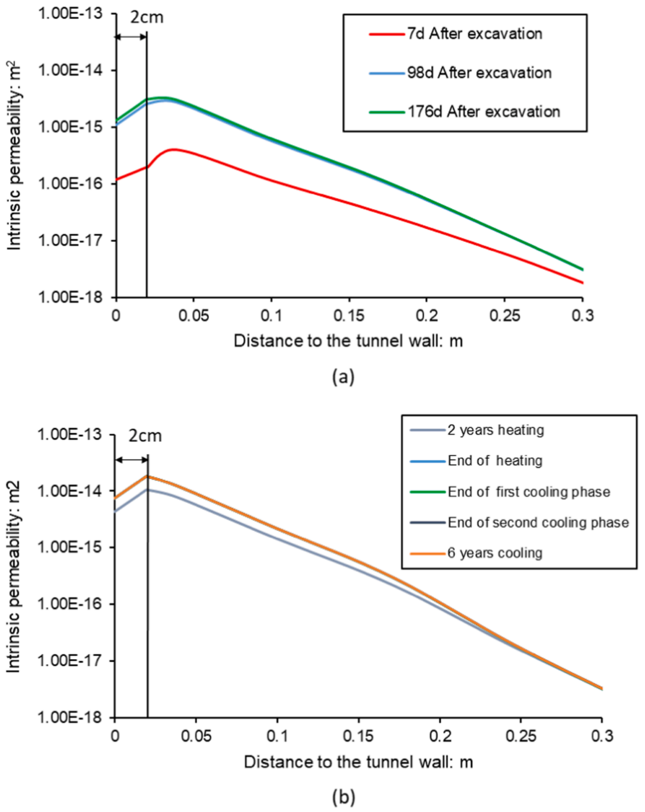

Fig. 22. Distribution of computed permeability with horizontal distance to tunnel wall and at various times.

the initial porosity has been set to a high value (0.8) but less than one.

The dependency of both permeability and air entry pressure on porosity has been considered in order to model their evolution towards host formation values when the gap closes. Thus, the dependence of the retention curve on porosity has been taken into account by considering the following equation:

$$P(\phi) = P_0 exp(a(\phi_0 - \phi)) \tag{29}$$

where a is a material parameter. This function allows a low retention capacity for the gap to be used when it is open that evolves into a higher retention capacity as the gap closes. The laws for vapour transport are the same as those for the rock but corresponding to a very large porosity. Fourier's law (Eq. (27)) is used to describe heat flow across the gap. The variation of thermal conductivity as the gap becomes more saturated is given by:

$$\lambda = \lambda_{sat} S_l + \lambda_{dry}(1 - S_l) \tag{30}$$

where $\lambda$is the thermal conductivity, $\lambda_{sat}$is the thermal conductivity of the water-saturated porous medium, $\lambda_{dry}$is the thermal conductivity of the dry porous medium and $S_l$is the degree of saturation. Heat transport by advection is considered automatically by the coupled formulation.

3.2.3. Steel casing

According to HLW disposal cell reference concept, an API5L steel grade with a high yield strength (above 450 MPa) is selected for the casing to reduce the risk of Stress Corrosion Cracking (Bumbieler et al., 2015). For ALC1604 experiment, casing and insert have been made of structural steel having a yield strength of 235 MPa and elastic properties similar to those of API5L steel. The casing is considered to be linear thermo-elastic with parameters E, ν and α for Young's (elastic) modulus, Poisson's ratio and the coefficient of thermal expansion, respectively.

The numerical analyses presented in this paper have been performed using the computer code Code_Bright (Olivella et al., 1996). It is a finite-element code (with some finite volume features) developed in-house for performing coupled THM analyses involving both saturated and unsaturated porous media.

4. Numerical simulation and comparison with test results

4.1. Features of analysis and material properties

In order to interpret the observed behaviour, a series of finite element simulations have been performed. To incorporate the anisotropic features of COx claystone and the in-situ stress state anisotropy a three-dimensional coupled THM analysis was performed. The model domain and the finite element mesh used are depicted in Fig. 7 where the reference system of axes is indicated. Axis y is in the vertical direction and axes × and z define the horizontal plane; axis z corresponds to the axis of the tunnel. The origin of coordinates is located at the beginning of the microtunnel (see also Fig. 1). The dimensions of the model are 50 m × 50 m × 50 m. The distance of the microtunnel wall to the boundary is 25 m, which corresponds to the distance from the

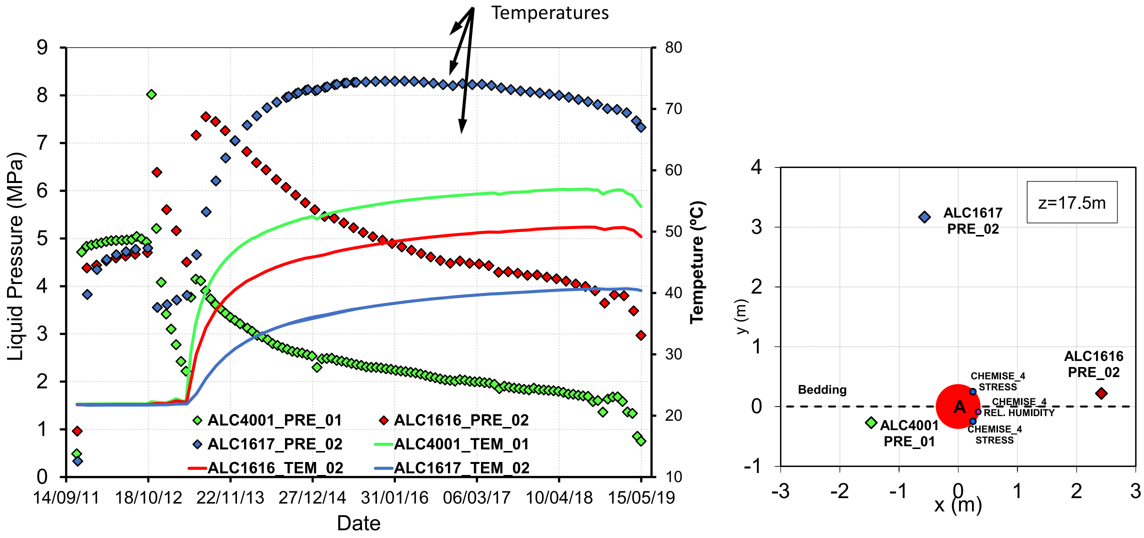

Fig. 23. Pore pressure and temperature evolution measured in sensors ALC1616_PRE_02, ALC1617_PRE_02 and ALC4001_PRE_01 located on the same section as the heaters (17.5 m from the tunnel entrance).

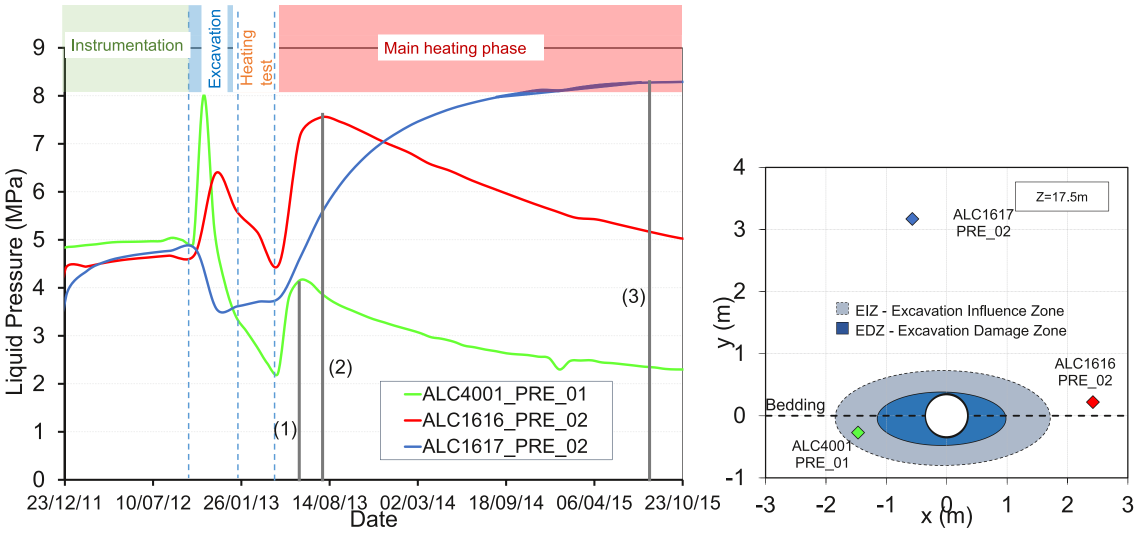

Fig. 24. Pore pressure evolution in sensors ALC1616_PRE_02, ALC1617_PRE_02 and ALC4001_PRE_01 (z = 17.5 m deep from the tunnel entrance).

microtunnel axis to the gallery GRD. Naturally, the model also incorporates the geometry of the casing and the air gap between the casing and the COx claystone (Fig. 8). In accordance with the experimental arrangement, the casing is supported by the bottom of the excavation, so the width of the gap is not uniform (Fig. 8). The mesh contains 3312 tetrahedral elements and 6720 nodes; it has been refined near the gallery and near the microtunnel, in order to be able to deal with the high temperature and pore pressure gradients in this zone.

An initial constant temperature of 21.8 °C has been assumed throughout the geometry. An anisotropic lithostatic initial stress distribution has been prescribed. Hydrostatic distribution of water pressure was initially defined, with a value equal to the field value (4.7 MPa) at test level. Values at experiment level are 12.7 MPa, 16.2 MPa and12.4 MPa (Wileveau et al. 2007) for the vertical, the major and minor horizontal components, respectively (Fig. 9).

For the two lateral surfaces, different boundary conditions are selected. The surface which corresponds to the cavities GAN and GRD assumes a constant stress boundary, whereas the condition of constrained lateral displacements is adopted at the opposite lateral boundary. Although galleries GAN and GRD are not geometrically represented in the mesh, the observed variation of temperatures and pore pressures are applied as boundary conditions at their locations. A prescribed liquid pressure (- 0.1 MPa) was applied to the excavation surface to represent the process of ventilation (Fig. 9). Heat power was applied as a thermal flux in the microtunnel. 90% of the heat power was applying uniformly in the zone of the heaters. The remaining 10% power was applied in the open air-filled zone between the heaters and the insert in order to reproduce in an approximate manner the effects of radiation and air thermal convection. The partition of the total heat flux was calibrated based the temperature measurements in the zone.

. The numerical analysis has simulated the various phases of the experiment, as listed in Table 1.Since the main objective of the analysis was to interpret the test observations rather than prediction, a number of key COx claystone parameters were calibrated from field observations. Table 2 contains the thermal, thermomechanical, hydraulic and petrophysical parameters for the host formation and their sources. The permeability values have been obtained from the back-analysis of the measured evolution of pore pressures in the test.

An appropriate interpretation of thermo-hydraulic coupling requires the thermal field to be well represented over the entire field. To this end, the value of the thermal conductivity of the COx claystone needs to be known as precisely as possible. Heat transport by advection is insignificant in low permeability media such as COx claystone, and therefore heat conduction is the only major mechanism for thermal transportation (Gens et al., 2007). Furthermore, the region remains saturated, and porosity changes are minor. Consequently, couplings from the hydro and mechanical components to the thermal problem are very weak and purely thermal analysis is sufficient to obtain the distribution and evolution of temperatures throughout the domain. Back-analysis of the observed test temperatures throughout the rock has been performed using 3D thermal analyses. The optimal values of thermal conductivity obtained are 2.05 W/(mK) in the direction parallel to bedding and 1.33 W/(mK) in the direction perpendicular to the bedding. They are in the range of variation obtained by back-analysis of TED experiment (Garitte et al. 2014).

Model parameters for the mechanical constitutive model are mostly based on those reported by Mánica et al. (2017) listed in Table 3. Rock strength anisotropy was defined by adopting scaling factors $c_N = 1.33$ and $c_S = 1.0$, selected to obtain a reasonable configuration of the damaged zone. Bedding planes are horizontal and, therefore, the anisotropy axis is vertical. In accordance with measurements of wave velocities in cubic samples (Armand et al., 2013), the ratio between horizontal and vertical Young's modulus has been set to 1.3.

Mechanical and thermal properties of the steel casing are listed in Table 4 whereas Table 5 summarises the gap parameters.

During the initial thermal “calibration work, two 2D plane strain analyses have been performed to anticipate and complement the resuts of the more time-consuming 3D simulation. The model domain, finite element meshes and main boundary conditions (B.C.) adopted are depicted in Fig. 10. The analysis A1 was run for the section located at a distance into the tunnel of z = 17.5 m (Cross-section across the centre of Heater 3) which is the location of the three boreholes that contain six temperature sensors and piezometers. A second analysis, A2, was performed with a different heat flux value for the section located at a distance into the tunnel of z = 13 m, which is the location of three boreholes that contain 14 temperature sensors and piezometers. Material parameters of the two-dimensional analyses are the same as in the 3D computation. A preliminary two-dimensional analysis of this test has been reported in Tourchi et al. (2019a, b).

4.2. Thermal results

A systematic comparison between simulation results and measurements has been made for each sensor. The temperature has been compared on the vertical cross-sections orthogonal to the cell as well as along each borehole containing temperature boreholes. The comparison

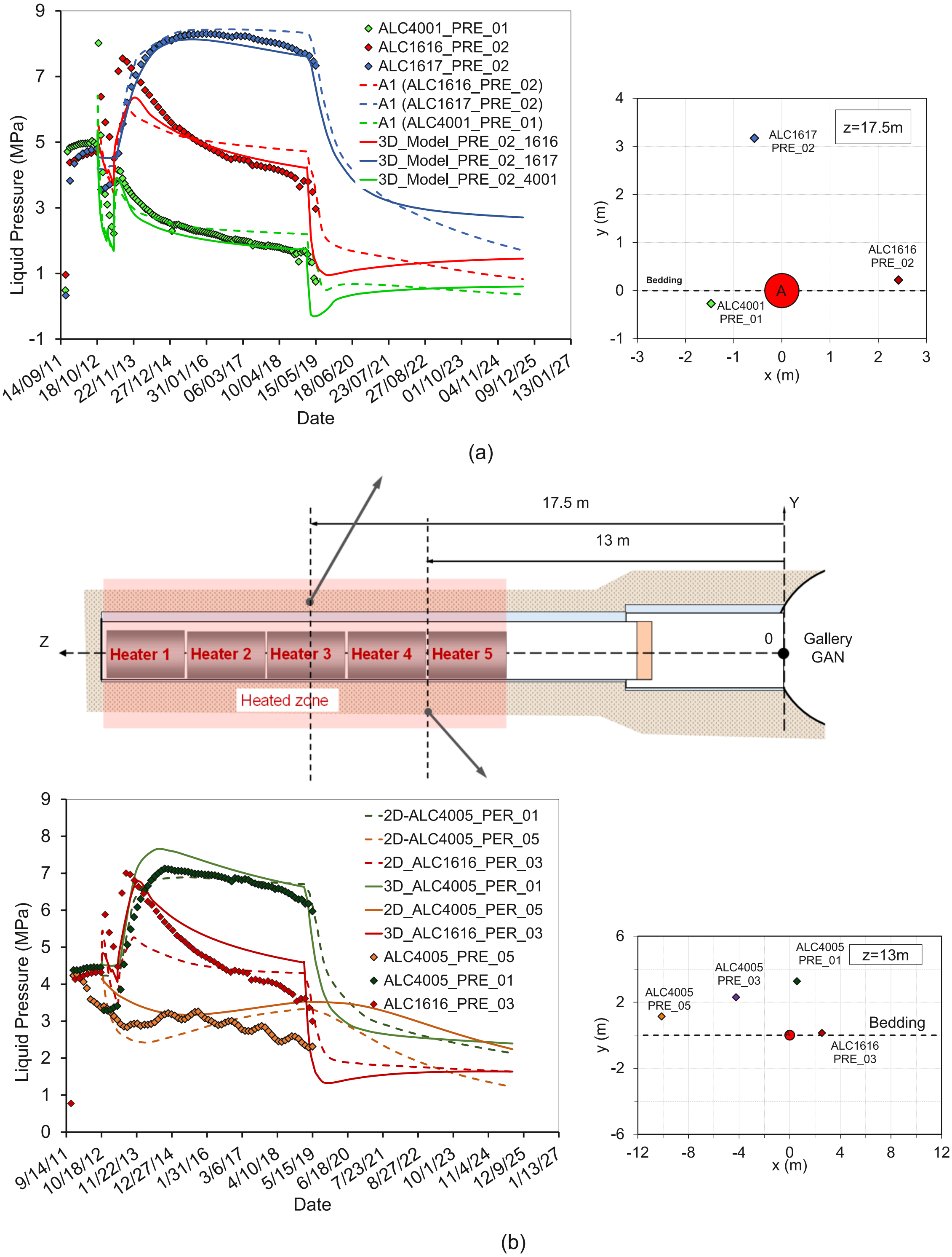

(a)

(b)

Fig. 25. Evolution of pore pressure increments at various points in the COx claystone: observed and computed results.

between the numerical results of the final 3D modelling and the measurements at all the sensors in the host rock, on the steel casing and within the gap is reported in (Tourchi et al., 2019c; Tourchi, 2020). There were three temperature sensors in section z = 17.5 m and seven sensors in section z = 13 m, located at different orientations with respect to the bedding plane. The observed evolution of temperatures at these two sections is shown in Fig. 11 and compared with the results of the 2D (dotted lines) and 3D (continuous lines) analyses. It can be noted that, after about one year of heating, temperatures generally rise very slowly throughout the COx claystone. Moreover, anisotropic effects are noticeable; temperature along the bedding increases more rapidly than in the orthogonal direction. As the thermal conductivity is back-calculated from 3D thermal analyses, it is not unexpected that the 3D THM captures well temperatures variations at all sensors. It is worth noting that the observed stabilization of temperatures at the end of the heating phase (1st semester 2019) is well-captured by the 3D model but cannot be reproduced by the 2D models. This indicates that heat dissipation along the z-direction (direction of the tunnel) has a noticeable

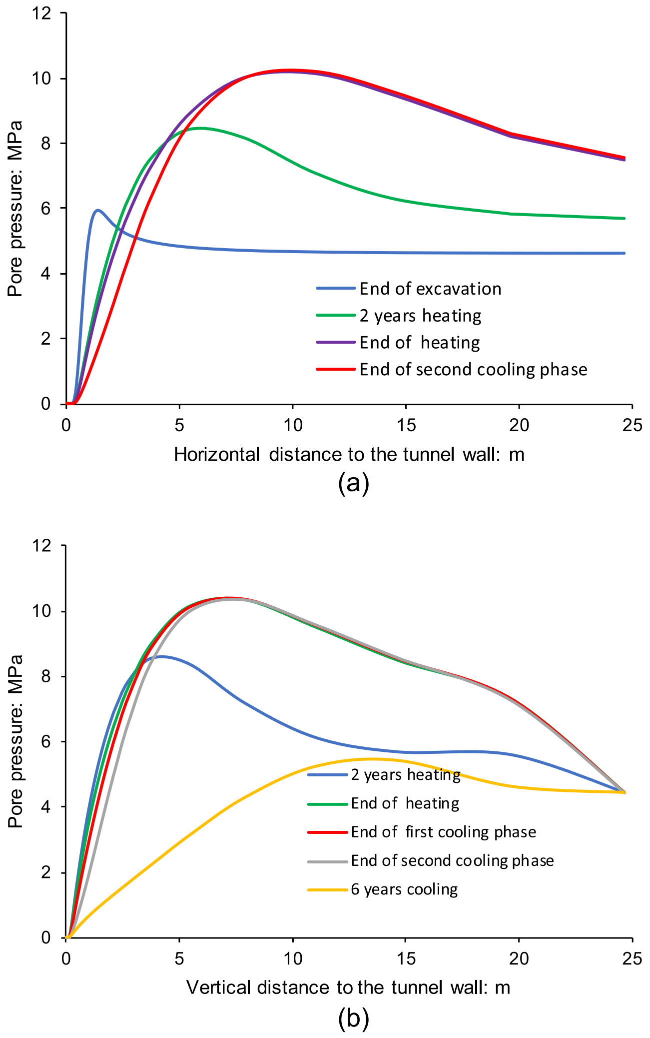

Fig. 26. Distributions of computed pore pressure increase at various times on section z = 17.5 m: (a) bedding plane direction; (b) perpendicular to bedding plane direction.

effect on the temperature field in the rock. In addition, the temperature measured along each borehole has been compared with the results of the model boreholes. For space reasons, only the temperature evolution of the sensors of boreholes ALC1616 and ALC4005 is shown in Fig. 12 and Fig. 13. The tendencies are very similar in both boreholes, higher temperatures for sensors located close to heaters and for sensors located along the bedding plane.

Fig. 14 and Fig. 15 show the contours of temperatures at different times. The anisotropic distribution of temperature is apparent with higher temperatures in the direction of the bedding planes.

Contours of temperatures at the end of the heating phase in planes x-z and x-y are presented in Fig. 16. Fig. 16a shows the extend of the thermal impact in the longitudinal direction and Fig. 16b illustrates again the effect of the higher thermal conductivity in the horizontal plane. Finally, Fig. 17 shows the distribution of temperatures of the casing. It can be observed that temperatures are somewhat higher at the bottom where the casing is in direct contact with the rock from the beginning.

4.3. Excavation damaged zone

Field observations have revealed that excavation operations induce damage and fracturing around the MHM URL galleries (Armand et al., 2014), creating an excavation induced fracture network, where significant changes in flow and transport properties take place. Tsang et al. (2005) gave a definition of the so-called excavation damage zone (EDZ) based on transfer properties, mainly permeability, significantly affected to impact long-term safety calculations. The EDZ is identified as one of the critical issues affecting the long-term behaviour of the tunnel near-field (Blümling et al., 2007). However, the relationship between mechanical damage and permeability in clayey rocks is complex and not straightforward due to self-sealing. Armand et al 2014 show in the COx that the EDZ from the point of view of the Tsang definition represents only a part of the fractured zone induced during excavation, the one where the extension fractures are observed. In the rest of this paper, the damage zone represents the mechanical damage based on the cumulative plastic multiplier. Significant efforts have been made to simulate these experimental excavations (Seyedi and Gens, 2017) and to gain insights into the design of the actual repository. The observed configuration of the EDZ depends on the orientation of the excavation with respect to the anisotropic in-situ stress state. As stated above, the ALC1604 cell is parallel to the major horizontal stress σ_H and has a nearly isotropic stress state in the plane normal to the tunnel axis. Despite that, the EDZ extends further in the horizontal direction (Fig. 18), suggesting anisotropic characteristics of the rock mass. Fig. 18 shows the distribution of fractures around a similar microtunnel (ALC3005) excavated in COx claystone parallel to ALC1604 cell.

An estimate of the configuration of the excavation damaged zone can be obtained by plotting contours of the cumulative plastic multiplier as it is directly related to the magnitude of irreversible strains (

Fig. 19). Only values of plastic multiplier corresponding to equivalent plastic shear above parameter ξ_2 ((13 and Table 3) are plotted because the fractured zone is interpreted as the zone where localized features develop as a consequence of material softening (or post-peak) regime. It is interesting to note that the lateral extent of the shear fractures zone calculated for the ALC1604 micro tunnel (about 0.7 m) is very similar to that observed in microtunnel ALC3005 (Fig. 18).

Fig. 20 presents the computed plastic multiplier distributions at various times in section z = 17.5 m. The following times have been selected: one day (cell opening); 7 days (end of the excavation); 176 days (end of heating test); 985 days (two years heating); 2297 days (end of main heating phase); 2358 days (end of first cooling phase); 2455 days (end of second cooling phase); 4668 days (end of 6 years cooling). After seven days from the excavation, almost all the damage has developed in the zone where stresses are higher than the available anisotropic strength (Fig. 20a). Afterwards, the damage progresses very slowly as the result of creep, consolidation and heating (Fig. 20b). At the end of the heating phase, after six years, the size of the damaged zone has only marginally increased (Fig. 20c). After about six years of cooling, the EDZ has barely changed (Fig. 20d).

Fig. 21 shows longitudinal horizontal profiles of the plastic multiplier along the microtunnel for various times at points located at a distance of 4 cm horizontal from the microtunnel wall. Two different zones are distinguished in the figure: EDZ caused by excavation and EDZ extension during the heating phase. As shown in Fig. 21a, EDZ evolution from day 7 (end of excavation) to the day 176 is negligible. It means that the effect of time-dependent hydromechanical evolution of COx claystone does not affect the EDZ evolution around the microtunnel. However, it seems that the heating phase causes some additional plastic deformations due to the larger increase of pore pressure in the heated zone.. A 3D view of the damage distribution is shown in Fig. 21b.

Fig. 22 shows horizontal profiles of computed intrinsic permeability on the right side of the cell. They are the result of the dependence of permeability on plastic multiplier introduced in the model; the coefficient defining the dependence has been back analysed to reproduce the pore pressures around the excavation. Computed permeability reaches a maximum value near the cell wall where it increases five orders of magnitude during excavation and one additional order of magnitude during heating.

These values should not be considered as quantitatively accurate but

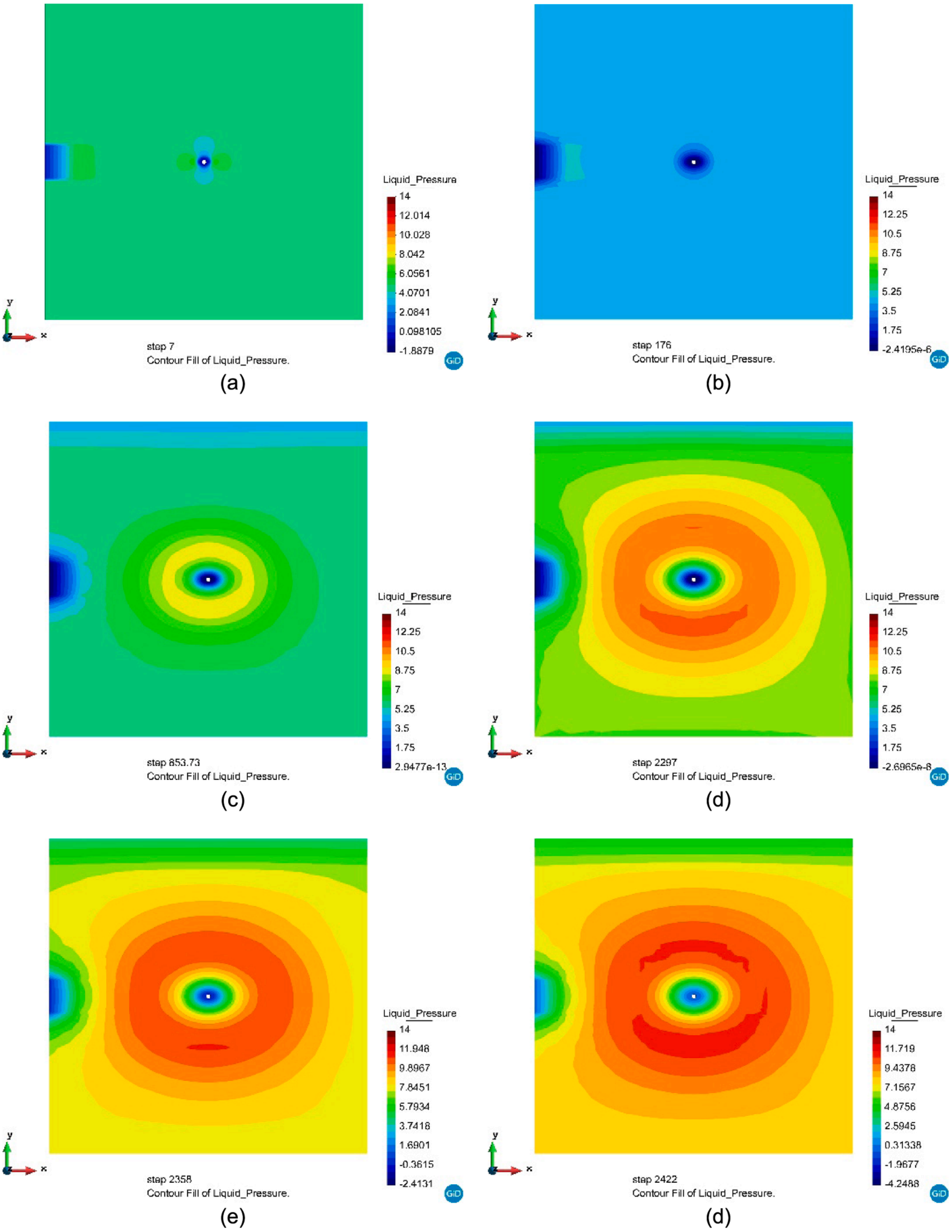

Fig. 27. Two-dimensional view of computed contours of equal liquid pressure (MPa) in a cross-section across Heater 3 for (a) 7 days (after excavation); (b) 176 days (end of heating test); (c) 853 days (two years heating); (d) 2297 days (end of heating) (e) 2358 days (end of first cooling phase); (f) 2422 days (end of second cooling phase).

essentially indicate a high permeable zone because of fracturing close to the excavation wall. An important factor for an adequate capture of the pore pressures measured in the rock during the ALC1604 experiment is the distance within the EDZ at which permeability experiences a change of at least one order of magnitude.

4.4. *Pore pressures*

An important aim of the experiment is to provide a good understanding of the pore pressure response during excavation and heating. Hydro-mechanical coupling and, particularly, the configuration and

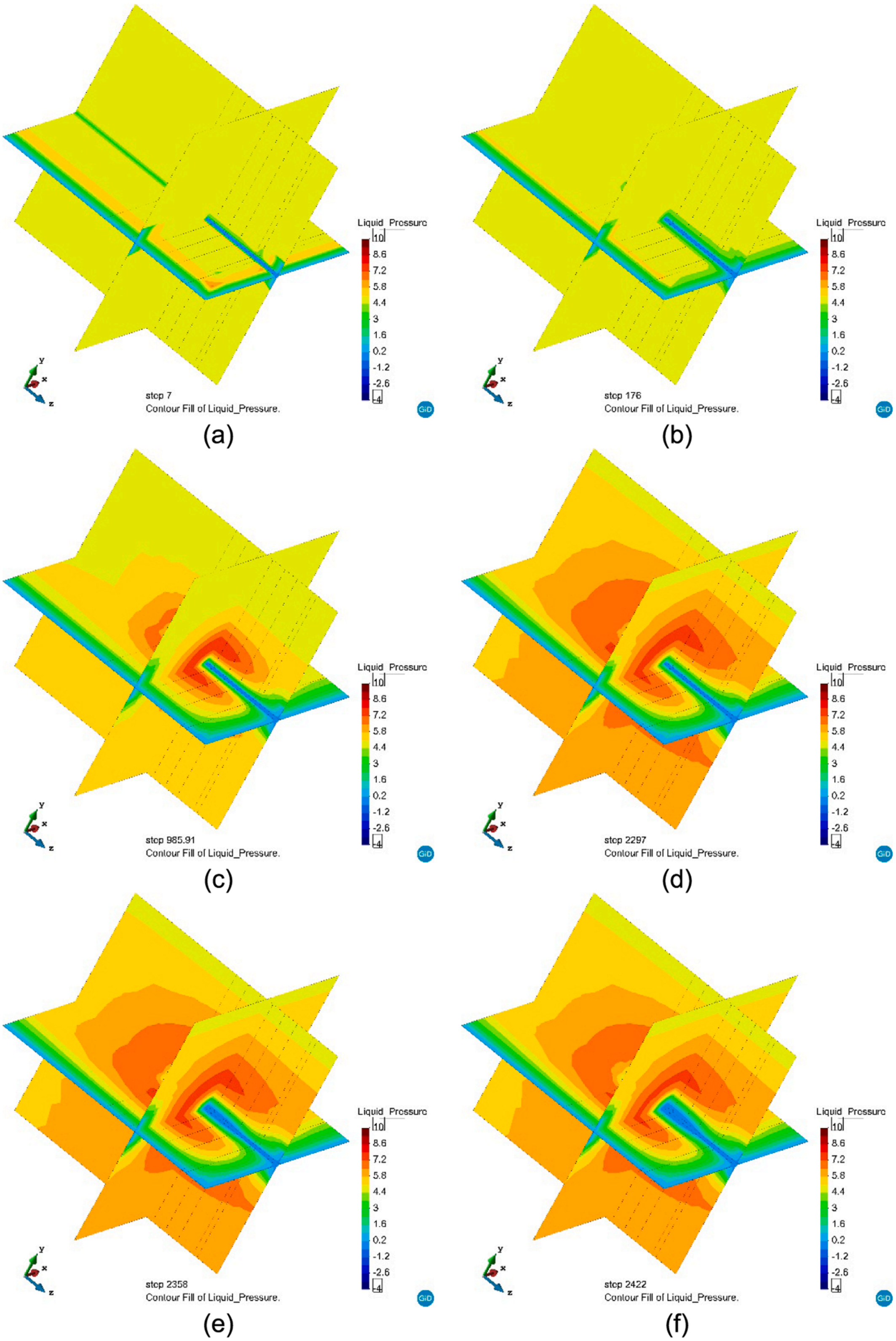

Fig. 28. Computed contours of equal pore pressure increase (MPa) for (a) 7 days (after excavation); (b) 176 days (end of heating test); (c) 958 days (two years heating); (d) 2297 days (end of heating); (e) 2358 days (end of first cooling phase); (f) 2422 days (end of second cooling phase).

extent of the EDZ, play a significant role in the pore pressure response. Fig. 23 shows the variation with time of temperatures and pore pressures, measured at sensors in section Z = 17.5 m deep.

The same graph is shown in Fig. 24, but focusing on the first days of the experiment. Water pressure raises as the excavation front approaches up to a value of about 8 MPa, i.e. 3.3 MPa above the initial value. Afterwards, pressure increase drops rapidly to 2 MPa as soon as the excavation front passes the corresponding measuring points. However, in the zone above the tunnel crown, pressures reduce which is linked to the geometry of the damaged zone around the cell being more

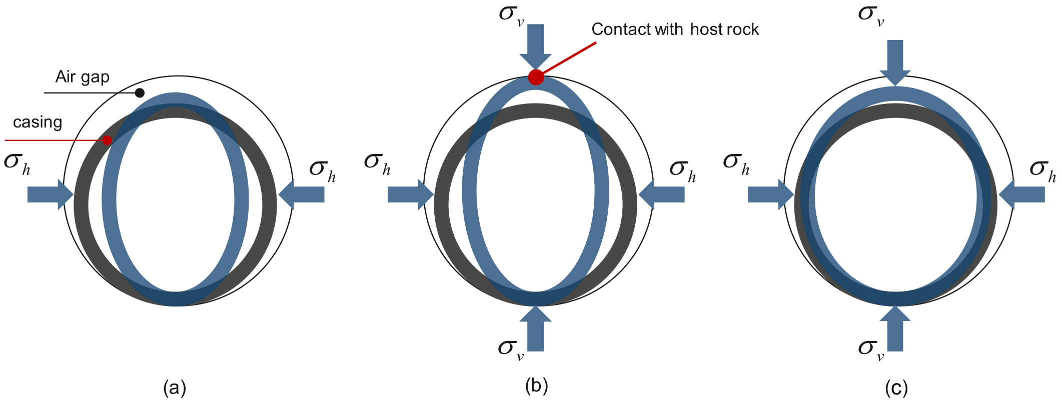

Fig. 29. Schematic representation of the three loading steps including (a) first loading step; (b) second loading step; (c) third loading step.

pronounced horizontally than vertically. The evolution of pore pressures at the borehole ALC1617 is also shown in Fig. 24 which is located in the vertical plane of the microtunnel (above the tunnel crown), 3.2 m away from the wall outside the EDZ. There is a slight increase in pore pressures as the excavation front approaches the measurement points.

The essential hydraulic phenomenon associated with thermal effects in COx claystone is the generation of the pore pressure due to temperature changes. The low permeability of COx claystone ensures that the resulting excess pore pressure does not dissipate rapidly. In this respect, interesting insights can be obtained examining a typical evolution of temperature and pore pressure, as presented in Fig. 23. As expected, temperature increases during the thermal stage trigger a significant rise of pore pressures; the greater the change in temperature, the stronger the response. The maximum pore pressure increase, in this case, is 7.5 MPa, a significant magnitude. It may also be observed that the progression in pore pressure does not precisely match the temperature: when pore pressure dissipation overcomes the thermal effect, the pore pressure stops increasing at a point although the temperature increases further. This phenomenon is especially apparent at two points located in the bedding plane (ALC1616 and ALC4001). Although in the 140 days after the beginning of the heating, the overpressure peak was observed on the horizontal plane of the tunnel, this peak was not achieved in the vertical plane above the crown of the tunnel for over 800 days. The difference in time taken to reach the overpressure peak in the vertical and horizontal planes is explained by the rock's anisotropic thermal and hydraulic properties (Fig. 23).

Fig. 25 presents a comparison between the results of the 3D analysis and pore pressure measurements at sections z = 17.5 and 13 m. The results of the two 2D analyses have also been added for comparison purposes. It is apparent that the pore pressure increase is reasonably well captured by the 3D model for both excavation and heating phases. The pore pressure rise recorded during the heating stage by sensor ALC1616_PRE_02 is, however, sharper than in the model. This could be due to the spatial discretization considered. The discrepancy is not observed in the two other sensors of the same sections.

The grey lines in Fig. 24 show the times of peak pore pressure in the section at z = 17.5 m. Peak times tend to increase as the distance to the microtunnel increases. These results from the combined effect of the movement of temperature rise outwards and pore pressure dissipation from the inner zones. This evolution can easily be observed in Fig. 26, where profiles of pore pressure at various times are plotted for two orthogonal directions. Differences between the two sets of distributions are apparent.

Finally, a general overview of the pore pressure field around the experiment is shown in Fig. 27 (2D) and Fig. 28 (3D). Movement of the locus of maximum pore pressure away from the microtunnel as time goes on is readily apparent. The maximum pore pressure computed by the model around the microtunnel during the heating phase is equal to 10.35 MPa and remains below the value of vertical stress. Figures also show the draining effect of the GRD gallery.

4.5. Thermomechanical behaviour of the casing

In the test, the evolution of the mechanical behaviour of the casing is monitored by convergence and local strain measurements on the inner face of the casing and Insert. The convergence measurement sections were installed in casing section 9, at a distance of 7 m into the tunnel, and insert 11 at 4 m from the entrance to the tunnel.

4.5.1. Convergences

Fig. 30 shows the overall evolution of convergence measurements of the casing since the connection of the sensors (48 days after the microtunnel excavation). Although the in situ stress field is almost isotropic, measurements in the cross-section (orthogonal to the microtunnel) exhibit an anisotropic load. This behaviour is consistent with the anisotropy of convergence measurements reported by Morel et al. (2013) for uncased HLW cells and Armand et al. (2013) for 5 m in diameter gallery. It can be observed that immediately after emplacement, the casing starts to converge in the horizontal direction, meaning that the theoretical initial annular air gap, which is about 3 per cent of the excavation diameter, disappears in this direction in less than 25 days.

Concerning the casing (cell body) response, three loading steps can be distinguished in Fig. 29 and Fig. 30. In the first step, the casing is subjected to the radial load in the horizontal direction corresponding to the maximum extension of EDZ. This loading results in the ovalization of the casing and a decrease in diameter in this direction. Ovalization is the evolution of the casing into an oval shape - i.e., non-circular - configuration. The second loading stage is characterized by strong increases in the casing convergence rate and thus its deformation by heating. In this step, the ovalization of the casing continues until it reaches the rock wall in the vertical direction. This loading step is followed by the third one, corresponding to a progressive decrease of the load anisotropy, resulting in a slight decrease of the ovalization. After 3 years of heating, a gradual increase of horizontal convergence seems to occur. After one year of heating, the convergence rate is less than 5×10^{-11} s^{-1} and ovalization already stopped.

The horizontal and vertical convergences of the insert in the cell head (sections11) are also shown in Fig. 30b. A similar short-term mechanical loading of the casing is observed. However, after five years of measurements, the convergence of the insert is not stabilised, which means that it is still in the first loading step mentioned above. The behaviour of the insert section shows no significant heating effect (the section is 6 m behind the heated zone). On this section, the loading scheme is the inverse of one of the casings, consisting of vertical convergence and noticeably equivalent horizontal divergence.

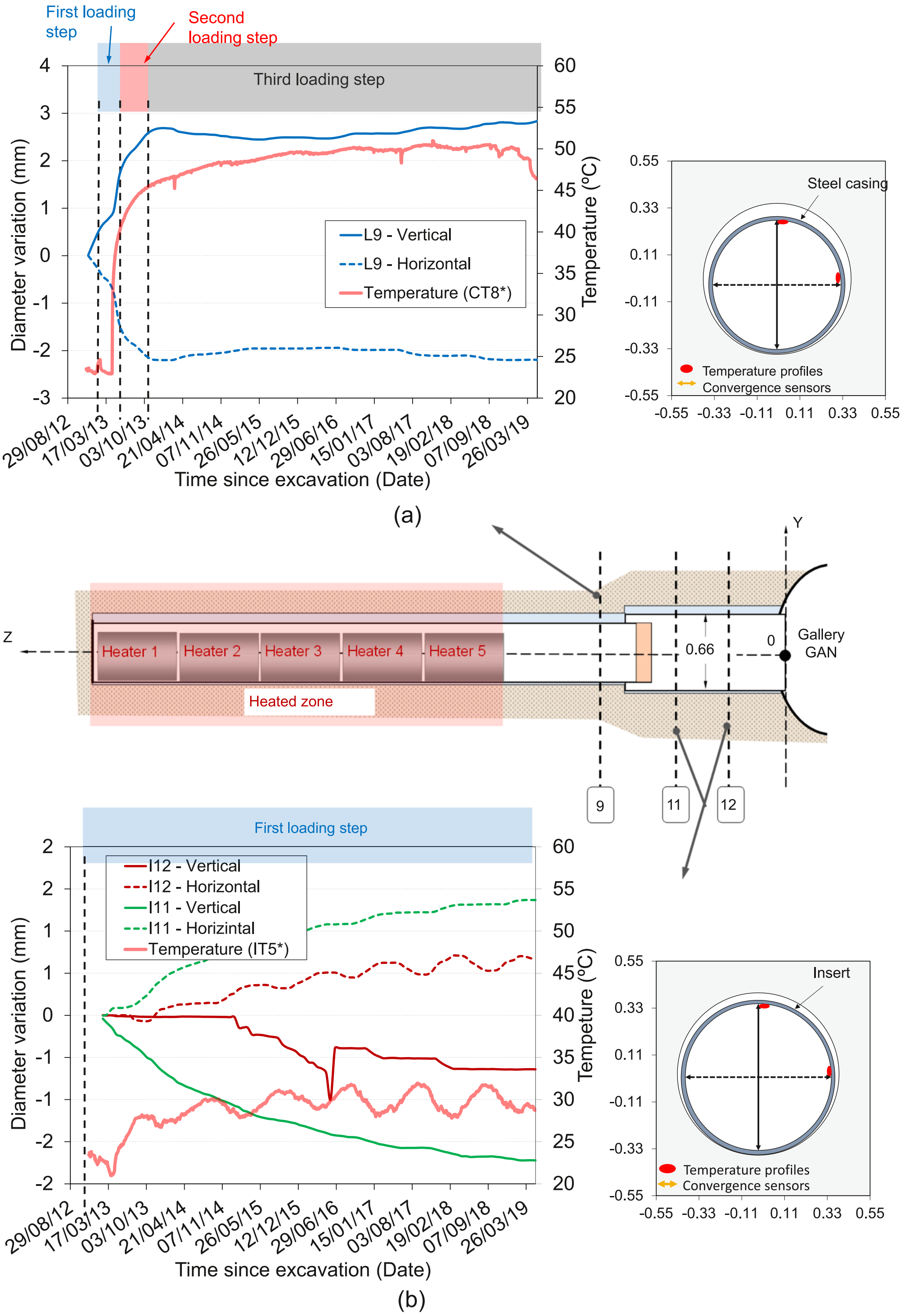

Fig. 30. Diameter variations measured on the casing section z = 7 m and the insert sections z = 2 m and z = 4 m.

Since the annular gap is much smaller around the insert (cell head) than around the casing (cell body), the insert is in contact with host formation at a very early stage. Besides, the mechanical strength of host formation is lower in the horizontal direction (bedding plane) due to EDZ anisotropy. Therefore, the insert tended to diverge horizontally.

Modelling of the casing has been described in section 3.2.1, 3.2.2 and 4.1 (see also Fig. 8). Properties for the steel and the gap are given in Table 4 and 5. Gap closure is modelled by an increase of three orders of magnitude for the Young modulus when the strain reaches a threshold which depends on gap initial aperture. Because of gap eccentricity, the value prescribed for the threshold varies along gap circumference. The Young modulus considered for the open gap is low but not null in order to account for the stiffness provided by the presence of debris fallen from the microtunnel vault after casing installation and evidenced by observations.

Fig. 31 presents a comparison between the results of the 3D THM analysis and convergence measurements of the casing for section 9 (depth of 7 m) and insert at section 11 (z = 4 m), since the connection of

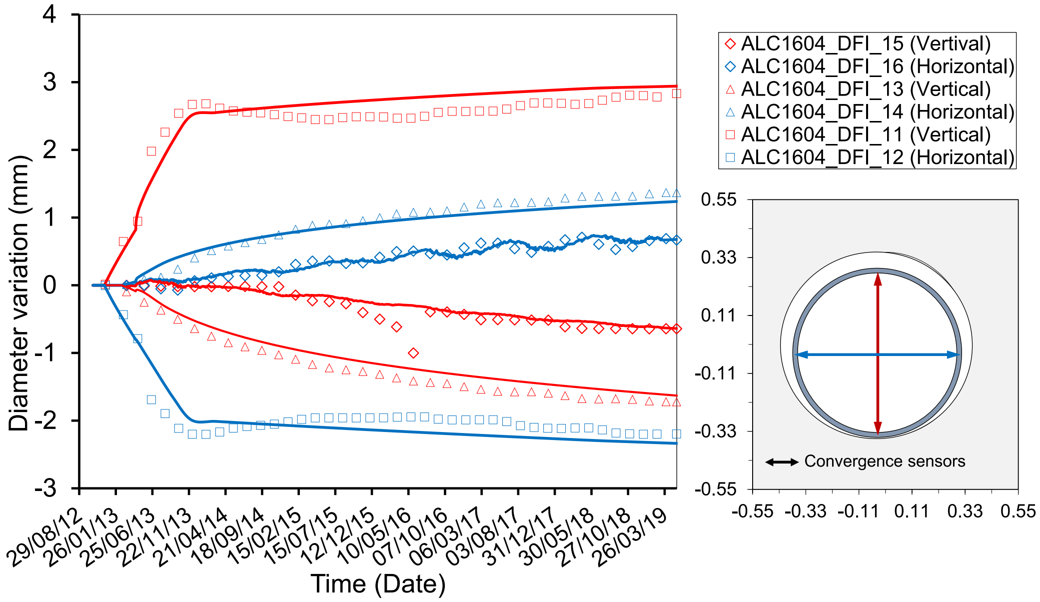

Fig. 31. Diameter variations measured (a) on the casing at a depth of 7 m; (b) on the insert at a depth of 2 m; (c) on the insert at a depth of 4 m (negative values correspond to convergence).

the sensors. It is apparent that the overall convergence behaviour is reasonably well captured by the model for the three loading steps as defined above, and the calculated results are in good agreement with the measured values. The model indicates that the ovalization during the first loading stage (waiting phase between excavation and heating phase) is controlled by the radial convergence of the microtunnel, in turn, governed by rock strength anisotropy. During the second loading stage (first months of heating), the model is able to capture the increase of ovalization rate, although with a slight underestimation. This result indicates the preponderant role of thermal expansion on the convergence rate but also suggests that additional effects not accounted for by the model, such as the dependency of strength on temperature, may have a marginal incidence. After 7 months of heating, the model predicts contact between casing and host formation, in a consistent way with observations. Afterwards, during the following 6 years of heating, the response of the casing enters in the third loading stage, characterized by full contact between casing and host formation. The reasonable reproduction by the model of the convergence rate during the latter stage provides further support on the capability of the constitutive law to capture the efforts applied by the rock on the steel lining during thermal pressurization and pore pressure dissipation. It is moreover interesting to note that the reversal of ovalization observed in section 11 at the insert is well-captured by the model and explained by the smaller gap thickness around the insert and the much earlier contact between casing and host formation at microtunnel vault than on lateral sides.

More information from the numerical analysis is given in Fig. 32 in terms of displacement contours and displacement vectors in a section across Heater 3 (section 17.5 m) at various times. The anisotropic load distribution and ovalization of the casing are apparent in the figures. The figure also shows that the casing keeps deforming during the cooling phase, as a result of creep. Deformation is not symmetric because of the presence of the GAN gallery on one side of the model. From a general point of view, the model shows to be capable of predicting both qualitatively and quantitatively the phenomena involved.

5. Conclusions

A full-scale in situ heating test has been performed to simulate the conditions of high-level radioactive waste disposal in a deep geological repository excavated in Callovo-Oxfordian (COx) claystone. The test has provided, for a period of up to six years, a large amount of information concerning the thermo-hydro-mechanical behaviour of the COx claystone, casing and the gap. The model developed in parallel have moreover allowed to a more thorough understanding of the THM processes in an HLW disposal system and have provided information for improvement in the design.

The model is the outcome of the different simulations performed during the project, including:

(1). 3D thermal analysis aiming at back-analysing the COx claystone thermal parameters.
(2). 2D thermo-hydro-mechanical analysis for a preliminary interpretation of pore pressures around the experiment during the excavation and heating phases and deformation of the steel casing during heating.
(3). A 3D thermo-hydro-mechanical modelling of the in situ test.

One of the main features of the work is to use a comprehensive and complex model to perform the calculations of a deposition scheme. The model includes:

- An anisotropic viscoplastic hardening/softening constitutive law with creep to model the COx claystone.
- Transverse anisotropy for the host formation thermal conductivity, permeability and elastic stiffness.
- Porosity-dependent permeability and water retention curve.
- A dependency of permeability on rock damage.
- Thermal conductivity depending on the degree of saturation (for gap elements).
- Material parameters consistent with previous field and laboratory experiments or with values reported in the literature.

The ·3D analyses performed include:

- A representation of the experiment geometry, including the host formation, excavated microtunnel, steel casing, insert and the gaps between the steel casing and the rock, the steel casing and the insert and the insert and the rock.
- The simulation of the different stages of the experiment (microtunnel excavation, heating and cooling).

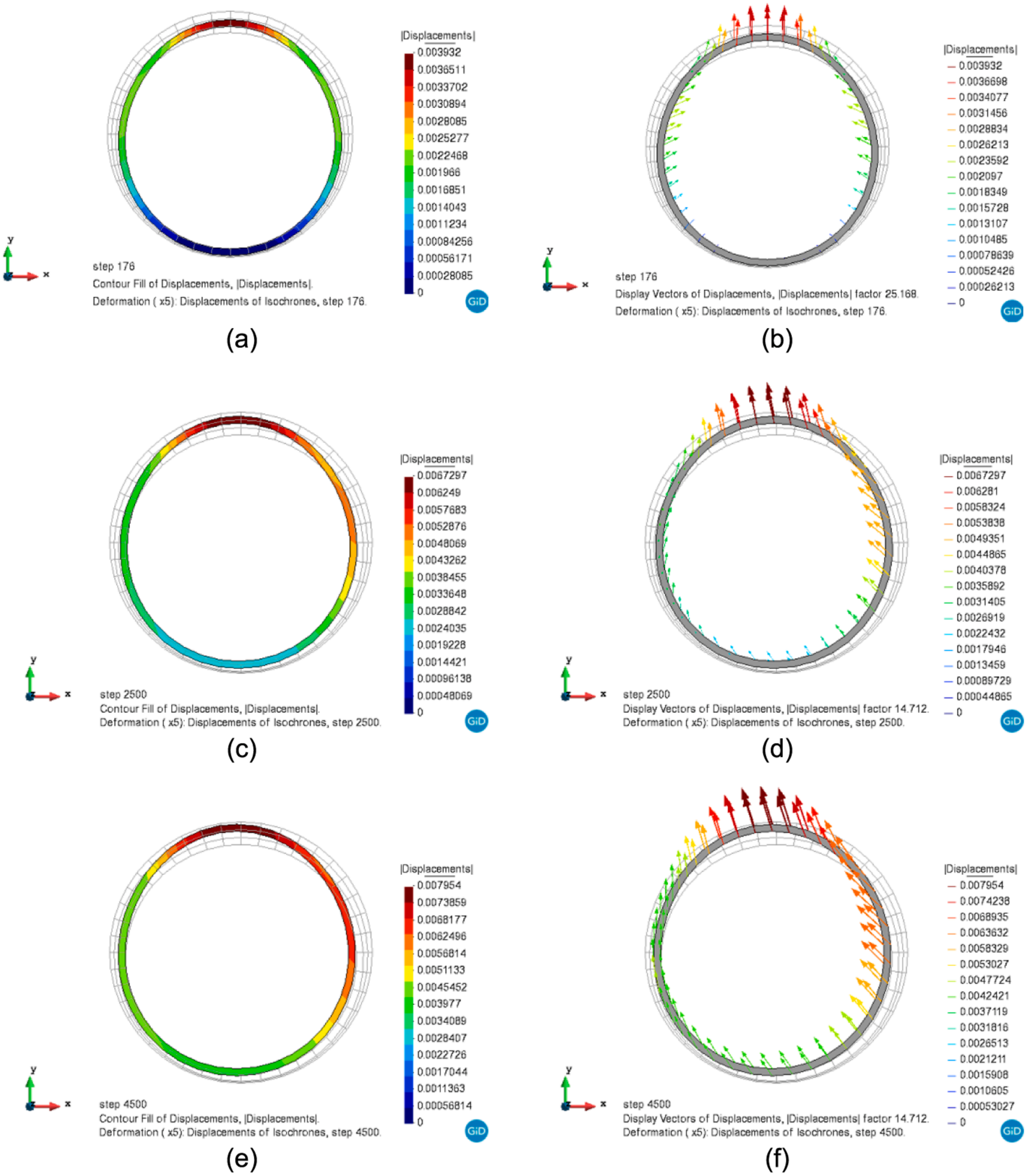

Fig. 32. Computed contours and vectors of displacement in casing at section 17.5 m for: (a) 176 days (before heating phase started); (b) (2500 days (six-year heating); (c) 4500 days (five years cooling).

- The thermo-hydraulic effect of the surrounding galleries.

The performance of 3D analyses has allowed the incorporation in the modelling of the mechanical, hydraulic and thermal anisotropy of the COx claystone as well as the anisotropic in-situ stress state. The mechanical model used has reproduced satisfactorily the configuration of the EDZ, a key feature that controls the mechanical and hydraulic response of the rock close to the excavation. The numerical analyses performed have been able to represent successfully the test observations and to provide a sound basis for the interpretation of the experiment.

The success in the reproduction of such complex in-situ heating test (ALC1604) shows the ability of the proposed THM model, which can be used for the prediction and reproduction of further in-situ experiments performed in the COx claystone.

CRediT authorship contribution statement

S. Tourchi: Conceptualization, Methodology, Software, Validation, Investigation, Formal analysis, Writing - original draft. **J. Vaunat:** Conceptualization, Methodology, Software, Validation, Investigation, Formal analysis, Writing - review & editing. **A. Gens:** Methodology, Validation, Investigation, Formal analysis, Writing - review & editing. **F. Bumbieler:** Conceptualization, Validation, Investigation, Data curation, Writing - review & editing. **M.N. Vu:** Conceptualization, Validation, Investigation, Data curation, Writing - review & editing. **G. Armand:** Conceptualization, Validation, Investigation, Writing - review & editing.

Declaration of Competing Interest

The authors declare that they have no known competing financial interests or personal relationships that could have appeared to influence the work reported in this paper.

Acknowledgements

The technical and financial support of the Agence Nationale pour la Gestion des Déchets Radioactifs (ANDRA) is gratefully acknowledged.

References

Armand, G., Bumbieler, F., Conil, N., et al., 2017. Main outcomes from in situ thermo-hydro-mechanical experiments programme to demonstrate feasibility of radioactive high-level waste disposal in the Callovo-Oxfordian claystone. J Rock Mech Geotech Eng 9, 415–427. https://doi.org/10.1016/j.jrmge.2017.03.004.

Armand, G., Leveau, F., Nussbaum, C., et al., 2014. Geometry and properties of the excavation-induced fractures at the meuse/haute-marne URL drifts. Rock Mech Rock Eng 47, 21–41. https://doi.org/10.1007/s00603-012-0339-6.

Armand, G., Noiret, A., Zghondi, J., Seyedi, D.M., 2013. Short- and long-term behaviors of drifts in the Callovo-Oxfordian claystone at the Meuse/Haute-Marne Underground Research Laboratory. J Rock Mech Geotech Eng 5, 221–230. https://doi.org/10.1016/j.jrmge.2013.05.005.

Auvray C (2004) Thermomechanical tests on opalinus clays of the Mont Terri, ANDRA Report C. RP OENG 4–239.

Bai M, Abousleiman Y (1997) Thermoporoelastic Coupling With Application To Consolidation. 21:121–132.

Bernier, F., Neerdael, B., 1996. Overview of in-situ thermomechanical experiments in clay: Concept, results and interpretation. Eng Geol 41, 51–64. https://doi.org/10.1016/0013-7952(95)00032-1.

Blümling, P., Bernier, F., Lebon, P., Derek Martin, C., 2007. The excavation damaged zone in clay formations time-dependent behaviour and influence on performance assessment. Phys Chem Earth 32, 588–599. https://doi.org/10.1016/j.pce.2006.04.034.

Bumbieler F, Necib S, Morel J, et al (2015) Mechanical And SCC Behavior Of An API5L Steel Casing Within The Context Of Deep Geological Repositories For Radioactive Waste. ASME 2015 Press Vessel Pip Conf 1–11. doi: 10.1115/PVP2015-45234.

Bumbieler, F., Plúa, C., Tourchi, S., Vu, M.-N., Vaunat, J., Gebs, A., Armand, G., 2021. Feasibility of constructing a full-scale radioactive high-level waste disposal cell and characterization of its thermo-hydro-mechanical behavior. Int J Rock Mech Min Sci 137, 104555.

Conil, N., Vitel, M., Plua, C., et al., 2020. In Situ Investigation of the THM Behavior of the Callovo-Oxfordian Claystone. Rock Mech Rock Eng 1–23.

De Bruyn, D., Labat, S., 2002. The second phase of ATLAS: The continuation of a running THM test in the HADES underground research facility at Mol. Eng Geol 64, 309–316. https://doi.org/10.1016/S0013-7952(01)00109-0.

François, B., Laloui, L., Laurent, C., 2009. Thermo-hydro-mechanical simulation of ATLAS in situ large scale test in Boom Clay. Comput Geotech 36, 626–640. https://doi.org/10.1016/j.compgeo.2008.09.004.

Garitte, B., Gens, A., Vaunat, J., Armand, G., 2014. Thermal conductivity of argillaceous rocks: determination methodology using in situ heating tests. Rock Mech rock Eng 47, 111–129.

Gens, A., Garcia Molina, A.J., Olivella, S., et al., 1998. Analysis of a full scale in situ test simulating repository conditions. Int J Numer Anal Methods Geomech 22, 515–548.

Gens A, Guimaraes L do N, Garcia-Molina A, Alonso EE (2002) Factors controlling rock clay buffer interaction in a radioactive waste repository. Eng Geol 64:297–308.

Gens A, Olivella S (2000) Non isothermal multiphase flow in deformable porous media. Coupled formulation and application to nuclear waste disposal.

Gens, A., Vaunat, J., Garitte, B., Wileveau, Y., 2007. In situ behaviour of a stiff layered clay subject to thermal loading: observations and interpretation. Géotechnique 57, 207–228. https://doi.org/10.1680/geot.2007.57.2.207.

IAEA, 2003. The Long Term Storage of Radioactive Waste. Safety and Sustainability.

Kim, J.S., Kwon, S.K., Sanchez, M., Cho, G.C., 2011. Geological storage of high level nuclear waste. KSCE J Civ Eng 15, 721–737. https://doi.org/10.1007/s12205-011-0012-8.

Mánica, M., Gens, A., Vaunat, J., Ruiz, D.F., 2016. A cross-anisotropic formulation for elasto-plastic models. Geotechnique 1–7.

Mánica, M., Gens, A., Vaunat, J., Ruiz, D.F., 2017. A time-dependent anisotropic model for argillaceous rocks. Application to an underground excavation in Callovo-Oxfordian claystone. Comput Geotech 85, 341–350. https://doi.org/10.1016/j.compgeo.2016.11.004.

Martin, C.D., Lanyon, G.W., 2003. Measurement of in-situ stress in weak rocks at Mont Terri Rock Laboratory, Switzerland. Int J Rock Mech Min Sci 40, 1077–1088. https://doi.org/10.1016/S1365-1609(03)00113-8.

Morel J, Bumbieler F, Conil N, et al (2013) Feasibility and behavior of a full scale disposal cell in a deep clay layer. In: ISRM International Symposium-EUROCK 2013.

Olivella S, Carrera J, Gens; A, Alonso E (1994) Non-isothermal multiphase flow of brine and gas through saline media. Transp Porous Media 15:271–293.

Olivella, S., Gens, A., Carrera, J., Alonso, E.E., 1996. Numerical formulation for a simulator (CODE_BRIGHT) for the coupled analysis of saline media. Eng Comput 13, 87–112. https://doi.org/10.1108/02644409610151575.

Picard, J.M., Bazargan, B., Rousset, G., 1994. Essai thermohydro- mecanique dans une argile profonde: Essai CACTUS. CEC, Luxembourg.

Seyedi, D., Armand, G., Besuelle, P., et al., 2015. A model benchmark exercise for numerical analysis of the Callovo-Oxfordian claystone hydromechanical response to excavation operations. In: In: 6. International Conference“ Clays in natural and engineered barriers for radioactive waste Confinement”, pp. 439–440.

Seyedi, D.M., Gens, A., 2017. Numerical analysis of the hydromechanical response of Callovo-Oxfordian claystone to deep excavations. Comput Geotech 85, 275–276. https://doi.org/10.1016/j.compgeo.2017.03.006.

Tourchi, S., 2020. THM analysis of argillaceous rocks with application to nuclear waste underground storage. BarcelonaTech (UPC).

Tourchi S, Vaunat J, Gens A, et al (2019a) Coupled thm analysis of long-term anisotropic convergence in the full-scale micro tunnel excavated in the callovo-oxfordian argillite. In: VIII International Conference on Computational Methods for Coupled Problems in Science and Engineering. Barcelona, pp 292–299.

Tourchi S, Vaunat J, Gens A, et al (2019b) Thermo-Hydro-Mechanical simulation of a full-scale steel-lined micro-tunnel excavated in the Callovo-Oxfordian Argillite. In: XIV International Conference on Computational Plasticity. Fundamentals and Applications COMPLAS 2019. Barcelona, pp 544–552.

Tourchi S, Vaunat J, Gens A (2019c) THM modelling of the ALC1604 experiment. Barcelona, Spain.

Tsang, C.F., Bernier, F., Davies, C., 2005. Geohydromechanical processes in the Excavation Damaged Zone in crystalline rock, rock salt, and indurated and plastic clays - In the context of radioactive waste disposal. Int J Rock Mech Min Sci 42, 109–125. https://doi.org/10.1016/j.ijrmms.2004.08.003.

Van Genuchten, M.T., 1980. A closed-form equation for predicting the hydraulic conductivity of unsaturated soils 1. Soil Sci Soc Am J 44, 892–898.

Wan, M., Delage, P., Tang, A.M., Talandier, J., 2013. Water retention properties of the Callovo-Oxfordian claystone. Int J Rock Mech Min Sci 64, 96–104.

Wileveau, Y., Cornet, F.H., Desroches, J., Blumling, P., 2007. Complete in situ stress determination in an argillite sedimentary formation. Phys Chem Earth 32, 866–878. https://doi.org/10.1016/j.pce.2006.03.018.

Zimmerman, R.W., 2000. Coupling in poroelasticity and thermoelasticity. Int J Rock Mech Min Sci 37, 79–87. https://doi.org/10.1016/S1365-1609(99)00094-5.